Applied Surface Science 680 (2025) 161434

Contents lists available at ScienceDirect

Applied Surface Science

journal homepage: www.elsevier.com/locate/apsusc

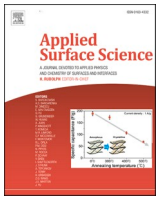

Full Length Article

Corrosion inhibitor from nature: Fundamentals of tannic acid inhibition for AA2024 alloy

Rubén del Olmo [a,b,*], Alexandre Bastos [a], Kiryl Yasakau [a], Alesia Sushkova [a], Raúl Arrabal [b], João Tedim [a]

[a] CICECO, Department of Materials and Ceramic Engineering, University of Aveiro, 3810-193 Aveiro, Portugal
[b] Department of Chemical and Materials Engineering, Faculty of Chemical Sciences, Complutense University of Madrid, 28040 Madrid, Spain

ARTICLE INFO

Keywords:
AA2024
Aluminium
Tannic acid
Corrosion inhibitor
Eco-friendly
Green inhibition

ABSTRACT

This study addresses the fundamentals of corrosion inhibition of AA2024 alloy by tannic acid (TA), a Cr-free and eco-friendly natural product. To this end, the AA2024 alloy was immersed in NaCl solution (50 mM) with different TA concentrations (0.1–10 mM) for 7 days. Surface (SEM, Raman, and SKPFM) and electrochemical analyses (EIS, PDP, and SVET) revealed mixed inhibition after 1 day of immersion in TA solution. Long-term immersion tests in TA solutions produced a tannate-rich oxide film on the surface. The films with low tannate content (formed in 0.1 and 1 mM TA) showed the highest stability and corrosion resistance.

1. Introduction

Driven by the need to reduce operating costs, fuel consumption, and increase payload capacity, the AA2024 (Al-Cu) alloy is the standard material for damage-tolerant and fatigue-sensitive applications in the aircraft industry [1]. However, despite its undeniable advantages, the AA2024 alloy is highly susceptible to localized corrosion in aggressive environments. This is mainly attributed to (i) the non-uniform distribution of copper within the Al solid solution (reaching up to 5 wt%), and (ii) the presence of cathodic Cu-rich secondary phases, *i.e.*, S-phase (Al_2MgCu), θ-phase (Al_2Cu), and Al-Cu-Mn dispersoids [2,3].

For this reason, AA2024 alloy is usually coated with a multilayer protection scheme, which consists of a pre-treatment (chemical conversion coating or anodic film) combined with multiple organic-based layers [4,5]. Among the most effective corrosion-inhibiting additives and pigments, Cr(VI)-derived species are the most widely used in all layers. However, it is well-known that Cr-based compounds are categorized as substances of very high concern (SVHC) by the *European Chemical Agency* (ECHA) [6] due to their high toxicity for humans and aquatic life, carcinogenic properties, and the economic costs associated with water treatment [4,7]. Several alternatives have been suggested to replace Cr(VI), some of which are presented in Table 1. However, most of these compounds are toxic and, in some cases, the inhibition is only noticed at high inhibitor/NaCl ratios.

The protection mechanisms of benzotriazole derivates, 8-hydroxyquinoline (8-HQ), vanadates, and gluconates typically involve the adsorption and/or precipitation on the alloy matrix and/or secondary phases. The interaction of these corrosion inhibitors (Table 1) is usually attributed to the presence of π-electrons and electronegative heteroatoms (nitrogen, oxygen, phosphorus, and sulfur), which act as adsorption centers to form stable surface complexes on the metal substrate [8–10]. Other inhibitors, such as cerium-based compounds, exhibit cathodic inhibition by precipitating on the Cu-containing secondary phases [11,12]. Another group of inhibitors, the lithium-based salts, are known to form a conversion-like coating on the AA2024 alloy, providing relatively efficient inhibition in saline media [10,13].

So far, the lack of alternatives underlines the need for available, eco-friendly, efficient, and cost-effective corrosion inhibitors for the AA2024 alloy [7]. An interesting approach that has been attracting significant attention in recent years is the use of natural products (*e.g.*, amino acids, essential oils, plant extracts, medicinal and biotechnological products) as corrosion inhibitors [14,15].

Among them, the use of tannin-derived molecules has attracted a great deal of attention [22,23]. The inhibitory effect of these compounds is associated with the presence of heteroatoms (such as oxygen), π-electrons, and conjugated bonds in the tannin structure, which favor their adsorption on different metallic substrates [23–26]. In detail, the stability of the inhibitor film depends on the specific functional groups,

* Corresponding author at: CICECO, Department of Materials and Ceramic Engineering, University of Aveiro, 3810-193 Aveiro, Portugal. Department of Chemical and Materials Engineering, Faculty of Chemical Sciences, Complutense University of Madrid, 28040 Madrid, Spain.
E-mail address: rubandom@ucm.es (R. del Olmo).

https://doi.org/10.1016/j.apsusc.2024.161434
Received 26 July 2024; Received in revised form 12 September 2024; Accepted 4 October 2024
Available online 5 October 2024

their aromaticity, and the interaction between the π-orbitals from the tannin and the d-orbitals from the steel substrate. Note that several studies also reported that tannins also act as rust converters, forming stable metallic-tannate networks with ferric ions [27–29]. These studies show that tannins can form chelates with Fe^{3+} at anodic sites, further enhancing their protective corrosion-inhibiting properties on different types of steel [30–32].

These findings suggest a promising research avenue for the AA2024 alloy since tannins are biodegradable, bioavailable, and non-toxic polyphenolic compounds with numerous applications in pharmacology and the food-production industries. Additionally, tannins can be extracted from different fruits, plants, and barks (such as bananas, grapes, chocolate, coffee, red wine, resins, and tea), making them readily available for mass production [22,23].

In the specific case of AA2024 alloy, the available literature is quite scarce since only a few tannin-derived molecules (*e.g.*, flavan-3-ol, mimosa-, and chestnut-derived tannins) have been studied as additives in anodizing baths and polymeric coatings [33,34]. Although these studies reported some improvement in the corrosion resistance of these coatings, the basis of the inhibitor effect of these compounds on AA2024 alloy is still unknown.

Therefore, the present work aims to study the corrosion inhibitor performance and corrosion mechanism of tannic acid on the AA2024 alloy as a function of its concentration in a saline medium. To this end, a commercial AA2024-T3 alloy was tested in various tannic acid/NaCl solutions (0.1–10 mM tannic acid in 50 mM NaCl) over different immersion times (up to 7 days). The characterization of the surface morphology and the interaction of tannic acid with the AA2024 alloy was assessed using optical microscopy (OM), scanning electron microscopy coupled with energy dispersive spectroscopy (SEM/EDS), scanning Kelvin probe force microscopy (SKPFM), optical profilometry, water contact angle (WCA) and Raman spectroscopy. The corrosion performance was quantified by electrochemical impedance spectroscopy (EIS), potentiodynamic polarization (PDP), and the scanning vibrating electrode technique (SVET).

2. Experimental part

2.1. Pre-treatment of AA2024 substrate and inhibitor solution preparation

Commercial AA2024-T3 alloy plates (wt.%: 3.8–4.9 Cu, 1.2–1.8 Mg, 0.3–0.9 Mn, < 0.5 Fe, < 0.5Si, < 0.25 Zn, < 0.15 Ti, < 0.10 Cr, and Al balance) were ground using successive grades of silicon carbide paper (up to P2500) and ethanol as a lubricant. Then, all plates were rinsed with distilled water and dried with air.

In this study, given the structural variations among different tannins, pure (purity: ≥ 99 %) solid-state tannic acid (TA (CAS: 1401-55-4); non-hydrolyzed) was used to ensure consistency and reproducibility in our experiments. Pure sodium chloride (NaCl) was obtained from Sigma-Aldrich (purity: ≥ 99 %). The study solutions were prepared in a 50 mM NaCl (Sigmaaqueous solution with the following concentrations of tannic acid: 0 M (blank), 0.1 mM, 1 mM, and 10 mM. Throughout the manuscript, these solutions will be referred to as blank, 0.1 mM TA, 1 mM TA, and 10 mM TA, respectively. The pH of all solutions was adjusted to 7 using a 0.1 M NaOH solution to simulate in-service conditions and ensure consistent benchmarking among the different TA concentrations. This adjustment enables a better understanding of the corrosion mechanism and aligns with the studied conditions reported in the literature (*Section 1*).

2.2. Interaction of Cu and Al with tannic acid

2.2.1. Immersion test of pure Cu and Al plates in tannic acid solution

The reactivity of the main components of the AA2024 alloy, Al and Cu, with tannic acid, was investigated separately using bare Al (99 % Al) and bare Cu (99 % Cu) plates. The metal plates (2 × 2 cm) were pre-treated by polishing using Buehler Cabinet sandpapers of grades P1000 and P2500 with ethanol as a lubricant, rinsed with ethanol, and dried with compressed air. Subsequently, both Cu and Al plates were immersed in 0.1 mM TA solution. The surfaces of both plates were monitored via visual analysis using a Nikon SMZ18 stereo microscope (*Section 2.4*).

2.2.2. Reactivity between Cu and Al cations with tannate anions: UV–Vis analysis

The reactivity of Cu and Al with tannic acid was verified in chloride solutions at a neutral pH range. Equimolar mixtures of tannic acid with pure $CuCl_2$ and $AlCl_3$ (Sigma-Aldrich) solutions were prepared at concentrations of 10 μM, 1 mM, and 10 mM. The mixtures were visually assessed and the filtered solutions (ϕ: 0.45 μm) were analyzed using UV–Vis spectroscopy (Sarspec Fabs Spectrophotometer™) across the wavelength range of 200–500 nm. The UV–Vis analysis was performed at 5 and 10 μM to fit within the upper limit of quantification of the equipment.

Table 1
Summary of the most efficient corrosion inhibitors for AA2024 alloy.

Inhibitor	Time (h)	pH/ Temperature (K)	Inhibitor/NaCl concentration (mM)	Efficiency (%)	Acute Toxicity LD50 Oral ^{rat} (mg/Kg)/ Carcinogenicity Toxicity ^{fish},mg/L	References
Benzotriazol derivates(2-mercaptobenzothiazole (2-MBT) , 2-mercaptoacetic acid, 4-mercaptobenzoic acid, benzotriazole, etc)	24–672	7/298	(5–50)/100	87–95	Equivocal tumorigenic agent (560)/ Harmful to aquatic life with long-lasting effects (25)	[10,16]
8-HQ	24	7	(3–50)/50	72–84	(n/a)/ Potentially mutagenic (18)	[9,17]
Cerium-based salts ($Ce(NO_3)$, $(NH_4)_2Ce(NO_3)_5$, $Ce_2(SO_4)_3$, $CeCl_3$)	144–600	7/298	1/10	96–97.5	Not identified (4200)/ Very toxic to aquatic life with long-lasting effects (0.3)	[11]
Ferrous and zinc gluconate	48–192	7/301	(10–42)/50	99	Very toxic to aquatic life (n/a)	[12,18]
Vanadate-based salts (NH_4VO_3, $NaVO_3$)	1	3–10/298	(3.2–320)/100	–	Very toxic to aquatic life (n/a)	[6,19,20]
Lithium carbonate	24	–/298	5/50	76	Known or potential hazard for reproductive toxicity (n/a)	[10]

+ Notes: 1 – The inhibitor efficiency is usually calculated by potentiodynamic polarization (PDP), electrochemical impedance spectroscopy (EIS), and/or mass loss after the immersion test.
2 – The toxicity data were reported in [6,21].

2.3. Electrochemical assessment of corrosion inhibition

2.3.1. Potentiodynamic polarization (PDP)

Potentiodynamic polarization (PDP) was performed on AA2024 samples after 1 and 1 day of exposure to the blank and the TA-based solutions at room temperature. The ground specimens, with a surface area of 0.4 cm^2, were placed in a three-electrode configuration connected to a Gamry potentiostat/ZRA Interface 1000. A saturated calomel electrode (SCE), and a platinum foil were used as reference and counter electrodes, respectively. To perform the test, all samples were polarized using a sweep rate of 1 mV/s within a range of −250 to +400 mV versus the open circuit potential (OCP). Each measurement was conducted in triplicate inside a Faraday cage to ensure repeatability. The authors calculated the corrosion potential (E_{corr}), and corrosion current density (i_{corr}) by triplicate using the Tafel extrapolation from the polarization curves [35]. Besides, both cathodic and anodic branches were considered to extrapolate their linear portions to determine the intersection, which corresponds to the i_{corr} and E_{corr} values. Note that the separate calculation of the anodic and cathodic parts was non-reproducible.

2.3.2. Scanning vibrating electrode technique (SVET)

The scanning vibrating electrode technique (SVET) was used to measure ionic currents in solution 100 μm above the sample's surface in both blank and 1 mM TA solution environments. AA2024-T3 samples (4 × 4.5 mm^2) were embedded in an epoxy matrix (Buehler EpoKwick FC) and their surfaces were grounded using SiC paper up to grade P1200. Measurements were performed with a commercial SVET system (Applicable Electronics Inc., USA) controlled by ASET software from ScienceWares Inc. (USA). The vibrating microelectrode was a Parylene C insulated Pt-Ir wire (Microprobes for Life Science, USA) with a Pt black sphere approximately 40 μm in diameter electroplated at the tip. The probe scanned 100 μm above the surface and vibrated at frequencies of 65 Hz and 108 Hz in normal and parallel directions to the surface, each with an amplitude of 10 μm. Only signals from normal vibration were used in this work. Each SVET map (50 × 50 points) required approximately 23 min to complete. Further details can be found in references [36,37].

2.3.3. Electrochemical impedance spectroscopy (EIS)

EIS was performed to evaluate the corrosion resistance of AA2024 alloy in the study solutions at room temperature. For this purpose, the aluminium plates with an exposed area of 3.4 cm^2 were placed in the same experimental set-up as described in *Section 2.3.1*, utilizing a three-electrode cell configuration connected to a Gamry potentiostat/ZRA 1000 interface. A saturated calomel (SCE), and a platinum foil were used as reference and counter electrodes, respectively.

All the EIS spectra were recorded at the open circuit potential (OCP) after different immersion times (1 h, 1 day, 2 days, 4 days, and 7 days) in the study solutions (blank, 0.1, 1, and 10 mM TA-based solutions). EIS measurements were performed in a frequency range from 10^5 Hz to 10^{-2} Hz, applying a sinusoidal signal with an amplitude of 10 mV (RMS) and 7 points per decade. For data analysis, impedance spectra were fitted using appropriate equivalent circuits with *Gamry Echem Analyst* software. The goodness of fit was ensured by chi-square values < 0.01.

2.4. Microstructural characterization of corrosion inhibition on AA2024 alloy

2.4.1. Scanning Kelvin probe force microscopy (SKPFM)

A commercial atomic force microscopy (AFM) Digital Instruments NanoScope IIIA multimode system with an Extended Electronic Module™ was used to study the topography evolution of alloy surfaces. Scanning Kelvin probe force microscopy (SKPFM) was used with the same system to quantify the Volta potential difference (VPD) between the AA2024 alloy matrix and intermetallic compounds before and after immersion in blank and 1 mM TA solutions.

For detailed principles, limitations, and result interpretation, refer to [38,39]. In brief, the lift height was set at 100 nm, and an AC voltage of 5 V was applied between the tip and sample to produce electrostatically induced oscillations of the cantilever. The Volta potential difference between the sample surface and the tip was measured using the nulling technique, with values reversed and normalized against a clean pure Ni substrate.

AFM/SKPFM maps were acquired with parameters set at 40 × 40 μm and 256 × 256 points. All measurements were conducted under room conditions (22–24 °C; 50–55 % relative humidity) using silicon probes coated with a Cr-Pt layer (Budget Sensors). AA2024 samples sized at 1 cm^2 underwent gradual polishing down to grade 0.25, followed by cleaning on a pad soaked with ethanol. The polished surface was exposed to the study solutions till 3 h of immersion. Afterwards, the surface was cleaned in a flow of Milli-Q water and dried in a stream of air. Prior to AFM/SKPFM measurements, samples were stored in a desiccator for 0.5–2 h.

2.4.2. Optical microscopy

The surface appearance of AA2024 samples during immersion in both blank and tannic acid-based solutions was continuously monitored using a stereo microscope Nikon SMZ18.

2.4.3. Scanning electron microscopy (SEM)

After 7 days of immersion in the study solutions, the surface morphology and chemical composition of the AA2024 alloy were analyzed using a Hitachi SU-70 scanning electron microscope (SEM) operated at 15 kV. The SEM was equipped with Quantax 400 energy-dispersive X-ray (EDS) microanalysis hardware.

2.4.4. Raman analysis

To analyze the chemical composition of the corrosion products, Raman spectroscopy was performed on the AA2024 surface after 7 days of immersion in the study solutions. The measurements were performed using a NT-MDT NTEGRA Spectra spectrometer (NT-MDT SI, Moscow, Russia), equipped with a Solar TII MS5004i monochromator (SOL Instruments Ltd., Minsk, Belarus), and a CCD Andor iDUS DU-420 detector (1024 × 128 pixels) (Oxford Instruments, Abingdon, UK). A 532 nm wavelength and 20 mW solid-state laser (with a 0.1 % ND filter attenuation) was used as an excitation source. Grating of 600 L/mm and acquisition times of 900 s were used.

2.4.5. Optical profilometry

Topographic images were obtained with an InfiniteFocusSL optical profilometer (ALICONA InfiniteFocusSL, Gmbh) to determine the roughness and texture differences of AA2024 after 7 days of immersion in the study solutions. Topographic information was analyzed with the IF-Measure Suite software to extract roughness parameters, such as Ra (arithmetic mean value in a roughness profile) and Sa (the difference in height of each point compared to the arithmetical mean of the surface).

2.4.6. Surface wettability

The wettability of corrosion product layers on AA2024 after immersion in the study solutions was evaluated using deionized with an OCA-20 goniometer (DataPhysics Instruments, Filderstadt, Germany) and the OneAttension software. The Laplace-Young method was used to determine the contact angle. Cited values are the average of 6 measurements (3 droplets on each of two replicate specimens).

3. Results

3.1. Short-term corrosion inhibition assessment of tannic acid on AA2024 alloy

3.1.1. Potentiodynamic polarization tests

Fig. 1 and Table 2 show the PDP curves and the electrochemical

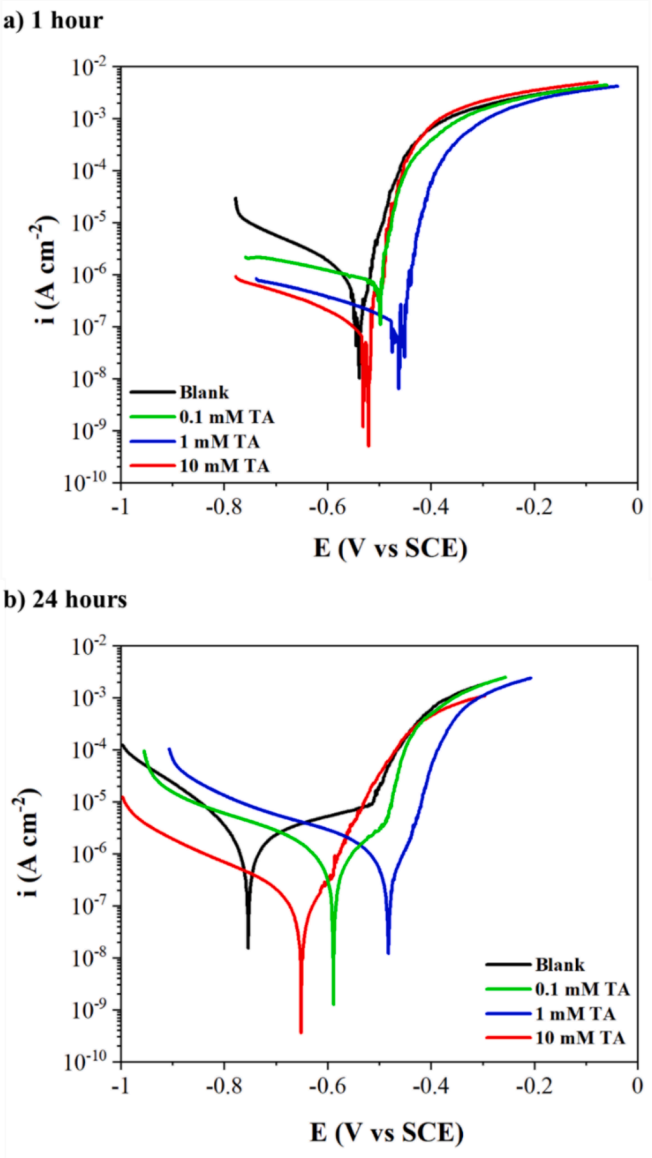

Fig. 1. Potentiodynamic polarization curves of AA2024 alloy after (a) 1 h and (b) 24 h of immersion in naturally aerated 50 mM NaCl solutions with different TA concentrations.

Table 2
The corrosion potential, current densities, and inhibition efficiency of tannic acid on the AA2024 alloy after 1 and 24 h of immersion in naturally aerated 50 mM NaCl solutions with different TA concentrations.

Solution	i_{corr} (A cm^{-2})	E_{corr} (mV) vs SCE	$E_{breakdown}$ (mV) vs SCE
1 h			
Blank	(3.20 ± 3.00) 10^{-7}	−541.0 ± 10.0	−538.0 ± 8.0
0.1 mM TA	(6.70 ± 1.70) 10^{-6}	−515.0 ± 30.0	−510.5 ± 20.0
1 mM TA	(1.60 ± 0.20) 10^{-7}	−478.0 ± 7.0	−468.0 ± 10.0
10 mM TA	(1.70 ± 0.50) 10^{-8}	−482.5 ± 1.0	−475.0 ± 3.0
24 h			
Blank	(2.60 ± 0.50) 10^{-6}	−762.5 ± 12.0	−512.3 ± 8.0
0.1 mM TA	(2.50 ± 3.00) $\cdot 10^{-6}$	−594.0 ± 37.8	−489.3 ± 27.0
1 mM TA	(1.20 ± 0.20)$\cdot 10^{-6}$	−533.0 ± 2.0	−438.2 ± 4.4
10 mM TA	(2.20 ± 0.10) 10^{-7}	−588.0 ± 38.0	−592.4 ± 28.5

parameters of the AA2024 alloy after 1 and 24 h of immersion in the study solutions, respectively.

It should be noted that special attention should be paid to the PDP technique when studying the AA2024 alloy due to its susceptibility to localized corrosion, which results in uncontrolled cathodic activity [8,10]. Therefore, PDP is herein used to address the short-term inhibitor performance in both cathodic and anodic processes as a comparative tool only.

After 1 h of immersion (Fig. 1; Table 2), the presence of tannic acid consistently shifts the corrosion (E_{corr}) and breakdown ($E_{breakdown}$) potentials to more positive values, thus denoting a corrosion rate decrease of the substrate [40,41]. However, attending to the i_{corr} value for the 0.1 mM TA solution, the results show a higher value compared to that of the blank solution (Fig. 1a). This result indicates that the 0.1 mM TA solution has a negligible inhibitor effect compared to 1 and 10 mM TA solutions (Fig. 1a; Table 2).

After 24 h of immersion (Fig. 1b; Table 2), all TA solutions show a great positive E_{corr} shift towards more positive values compared to the blank solution (Fig. 1a; Table 2). Notwithstanding, the lower i_{corr} values reported for 1 and 10 mM TA indicate that this is the optimal concentration range to achieve optimal corrosion inhibition (Table 2).

Note that for 10 mM TA, the negative $E_{breakdown}$ and the minor E_{corr} shift suggest that the excess of tannate anions may not promote a stable film under anodic polarization. This reduced protection could be due to the lower stability of the adsorbed layer and the complexation reactions between the aluminium cations and the polyphenol groups [40,42]. This has been shown in the literature, where the highest inhibitor efficiency is achieved in a specific concentration range (Table 1).

In the anodic branch (Fig. 1**b**), an increase in current density at more positive potentials is noted in all studied solutions. This is usually related to the S-phase dissolution (*i.e.*, pitting corrosion) and the onset of intergranular corrosion [8,43]. In the cathodic branch (Fig. 1**b**), solutions with 1 and 10 mM TA show a decrease in current density, suggesting that the interaction between tannic acid and cathodic Cu-rich particles is more efficient at these concentrations. Therefore, qualitatively, it can be inferred that 1 mM tannic acid is the minimal concentration required to achieve noticeable corrosion inhibition in the AA2024 alloy.

3.1.2. SKPFM analysis

To quantitatively address the short-term corrosion inhibition of TA on AA2024 alloy, SKPFM was used to analyze the response of the Al matrix and the S-phase (Al_2CuMg) after immersion in blank and 1 mM TA solutions. Fig. 2 shows the topography and Volta potential maps acquired for identical regions of the AA2024 alloy before and after 1 h of immersion in the blank solution.

After immersion in the blank solution, the topographic maps (Fig. 2**a, b**) show higher depth values, indicative of the dissolution of the aluminum matrix and the S-phase (Al_2CuMg) [44,45]. Besides, the Mean square surface roughness (Ra) of the surface increased from 6.9 ± 0.2 nm to 53.4 ± 10.3 nm after immersion. Additionally, immersion in the blank solution resulted in a significant rise in the matrix potential and a noticeable broadening of the VPD around the S-phase (Fig. 2**c,d**). These changes were attributed to the S-phase dealloying and copper redeposition around the dissolved S-phases [8,43,45,46].

In contrast, the topographical maps (Fig. 2 **e,f**) of AA2024 alloy immersed in 1 mM TA solution reveal (i) a consistent depth profile, and (ii) minor precipitates scattered over the surface (depicted as faint white dots in Fig. 2**f**). The Mean square surface roughness increased slightly from 5.5 ± 0.7 nm to 8.6 ± 1.0 nm.

These findings align with the Volta potential maps (Fig. 2 **g,h**) since no corrosion phenomena were detected in the AA2024 sample after 1 h of immersion in 1 mM TA solution. A notable increase in the VPD level of the Al matrix was detected, surpassing even the S-phase before immersion. Specifically, the potential shifted approximately 400 mV towards more positive values (Fig. 2**h**).

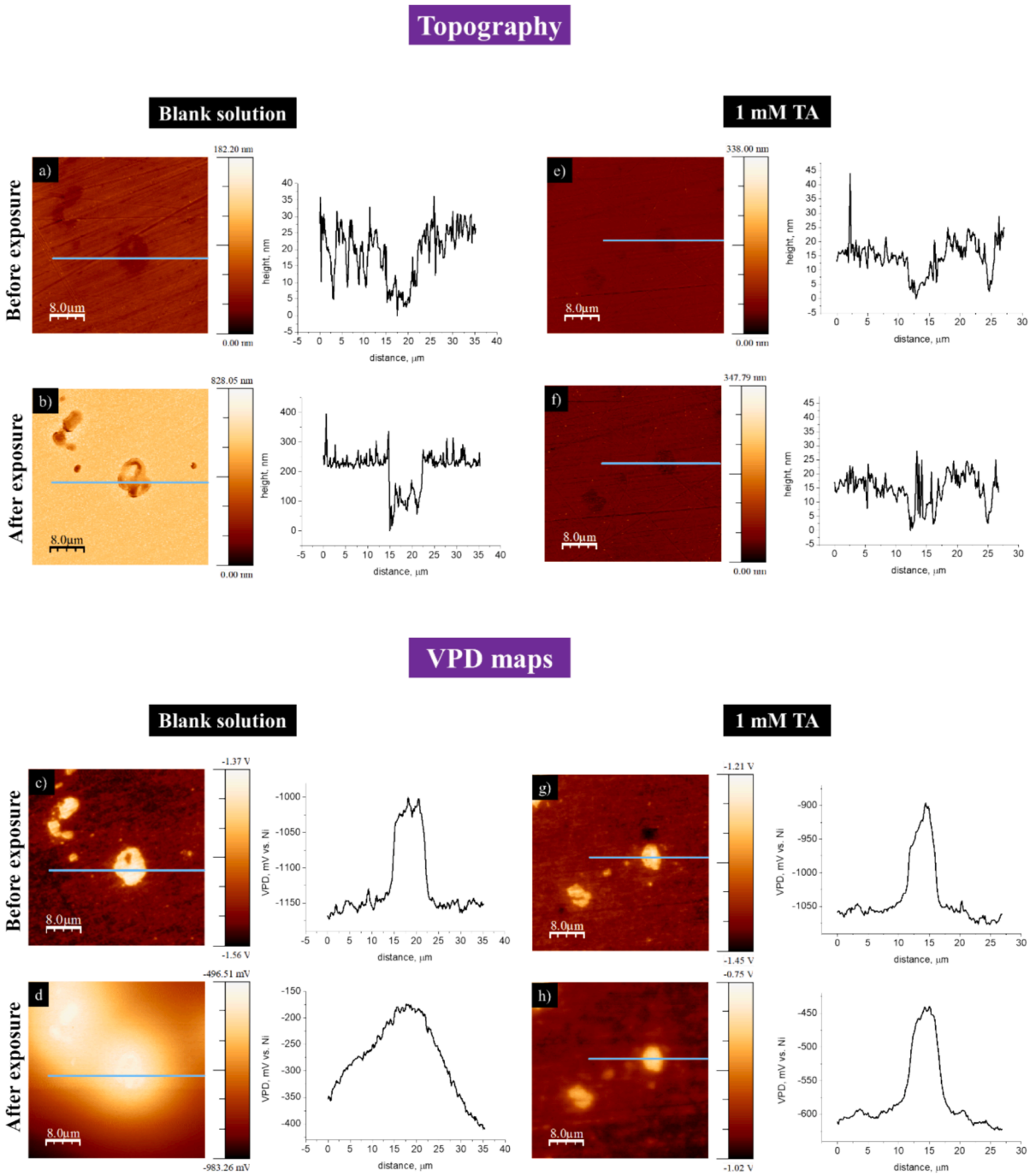

Fig. 2. (a,b) Topography and (c,d) Volta potential maps for AA2024 before and after immersion for 1 h in blank solution (50 mM NaCl). (e,f) Topography and (g,h) Volta potential maps for AA2024 before and after immersion for 1 h in 1 mM TA solution.

Note that similar results to those acquired after 1 h of immersion were obtained after 3 h of immersion (**Figure S1**).

After 3 h of immersion, the VPD shifts further to more positive values preferentially on the Al matrix, while VPD on top of the S-phase stays at the level close to established after 1 h of immersion (**Figure S1**). Besides, note that no VPD broadening was observed, thus indicating the passive behaviour of the S-phase at the early stages of immersion in the TA solution [45]. This is in agreement with the cathodic activity decrease observed in the polarization curves (Fig. 1).

To explain these findings, it should be noted that tannic acid in an aqueous solution at neutral pH is in the form of tannate anions [22,47]. Therefore, the observed differences in the topographic and VPD maps may be related to the interaction of tannate anions with the aluminum matrix and/or the S-phase at the early stages of immersion in the tannic acid solution. Interpretation of VPD changes is complex due to the combination of numerous factors, including the semiconducting oxide films and adsorbed species from the gas phase [48], dielectric layers [49], hydroxyl groups on the Al surface [50], the interaction of organic molecules with the surface [51,52], and S-phase dealloying [43], among others. Among them, the contribution of the negatively charged tannate molecules to a positive VPD offset is the most suitable explanation.

As was discussed by Yasakau *et al.* [52], VPD shifts positively when the dipole moment (defined as a combination of the molecular and chemical dipole moments) of an adsorbed organic layer is oriented toward the metal surface. This VPD increase was also reported on TiO_2 with negatively charged N719 dye adsorption [51]. Therefore, the

proposed adsorbed tannate-rich layer results in a negative charge located outside the molecular layer with a preferential surface-oriented dipole moment. To meet these conditions, either the chemical dipole (defined as the interaction between the functional groups of tannic acid) and/or the molecular dipole (representing the orientation of the molecule on the AA2024 surface) must be sufficiently strong. This suggests a strong interaction of the TA molecules with the surface. On that basis, although the available literature based on the interaction between Al and tannate anions is quite scarce, the chemisorption of tannate anions (Al-OR bonds from tannate anions) is the most suitable interaction expected [47,53].

3.1.3. SVET analysis

To assess the kinetics and electrochemical inhibition phenomena affecting the aluminium matrix and Cu-rich secondary phases, the AA2024 alloy was analyzed using the scanning vibrating electrode technique (SVET) during the first 24 h of immersion in both blank and 1 mM TA solutions (Fig. 3). SVET maps show regions of anodic activity (positive currents, shown in red) and cathodic activity (negative currents, shown in blue) across the AA2024 surface during the immersion period.

Optical images and SVET maps of the AA2024 alloy surface immersed in the blank solution (Fig. 3**a–c**) revealed (i) surface tarnishing due to the formation of corrosion products, and (ii) localized areas of high anodic activity. Note that these anodic peaks persisted in the same locations throughout the testing period, which typically indicates the presence of Cu-rich phases over the AA2024 surface [37]. This is in line with the VPD maps in the SKPFM analysis (Fig. 2**a–d**).

In contrast, the AA2024 sample immersed in the 1 mM TA solution (Fig. 3**d–f**) showed minimal surface brightness loss. Besides, the cathodic (blue) currents observed on the aluminium matrix after 1 h of immersion (Fig. 3**d**) were comparable to those measured in the blank solution after 24 h of immersion (Fig. 3**c**). Comparing these findings with those from the SKPFM test (Fig. 2**g, h**), it can be inferred that tannate anions delay aluminum dissolution in NaCl medium from the beginning of the immersion.

Regarding the electrochemical behaviour of Cu-rich secondary phases in 1 mM TA solution, the anodic (red) currents in localized areas were significantly lower (Fig. 3**d–f**) than those detected in the blank solution (Fig. 3**a–c**), even after 24 h of immersion.

To further investigate the interaction of tannate anions with the AA2024 alloy, pure Cu and Al plates were immersed in a 1 mM tannic acid (TA) solution for 72 h (**Figure S2**). On the Cu plate, a yellow-colored deposit and gradual surface darkening were observed after 72 h of immersion, while the Al plate showed a brownish color and microscopic precipitates after 48 h of immersion.

As later discussed in *Section 3.2*, the brown-colored layer observed on the Al plate can be attributed to tannate chemisorption on the Al matrix. Regarding Cu-rich secondary phases, research by Beccaria *et al.* [54] on pure copper demonstrated the chemisorption of tannate anions through a covalent bond between Cu and the phenolic group of tannic acid (Cu-OR). The authors also noted a low solubility of Cu-tannate complexes in artificial seawater (0.2 ppm at pH ~ 6.5 [55]), indicating efficient tannate chemisorption.

These observations would explain the reduced activity in localized regions in the AA2024 alloy immersed in 1 mM TA solution, as observed in the VPD and SVET maps. Note that upon closer examination of the 1 mM TA solution (optical images in Fig. 3**d–f**), several small black precipitates in the 1 mM TA solution were detected after 6 h of immersion. It is conceivable that these black precipitates result from the interaction between the free tannate anions in the solution with the Cu^{2+} and Al^{3+} ions from the AA2024 dissolution. As a result, insoluble Al- [47] and Cu-tannate [53,56] precipitates (**Figure S2**) may be formed in the solution.

To further elucidate the interaction between Al and Cu cations with tannate anions in saline medium, equimolar mixtures (10 μM, 1 mM, and 10 mM) of tannic acid with $CuCl_2$ and $AlCl_3$ were evaluated through UV–Vis spectroscopy (5 and 10 μM) (Fig. 4**a**) and visual observation (Fig. 4**b–g**).

UV–Vis analysis (Fig. 4**a**) revealed a decrease in the intensity of the characteristic tannic acid peak (276 nm assigned to the $\pi \rightarrow \pi^*$ transition by aromatic and C=O groups [57]) in the presence of $CuCl_2$ and $AlCl_3$ (10 μM). This finding confirms a reaction between tannic acid and the Al

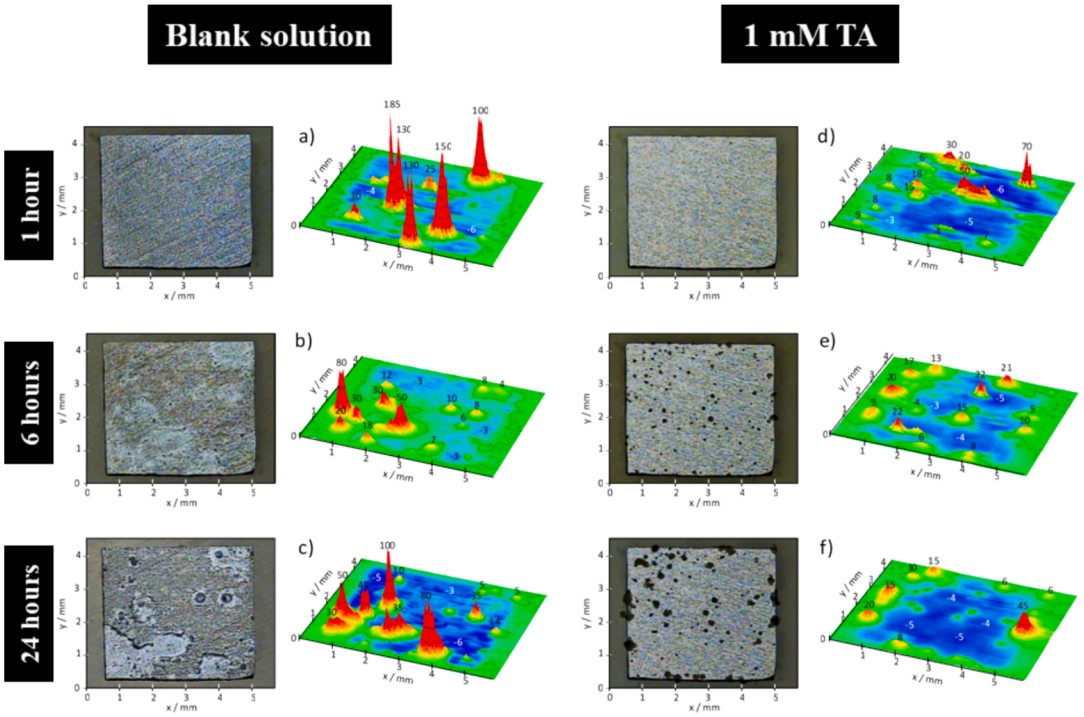

Fig. 3. Surface images and SVET maps of AA2024-T3 immersed in 50 mM NaCl (a-c) and 1 mM TA solutions (d-f). The maps were acquired after 1 h (a, d), 6 h (b, e), and 24 h (c, f) of immersion. The current density units depicted in the maps are μA cm^{-2}.

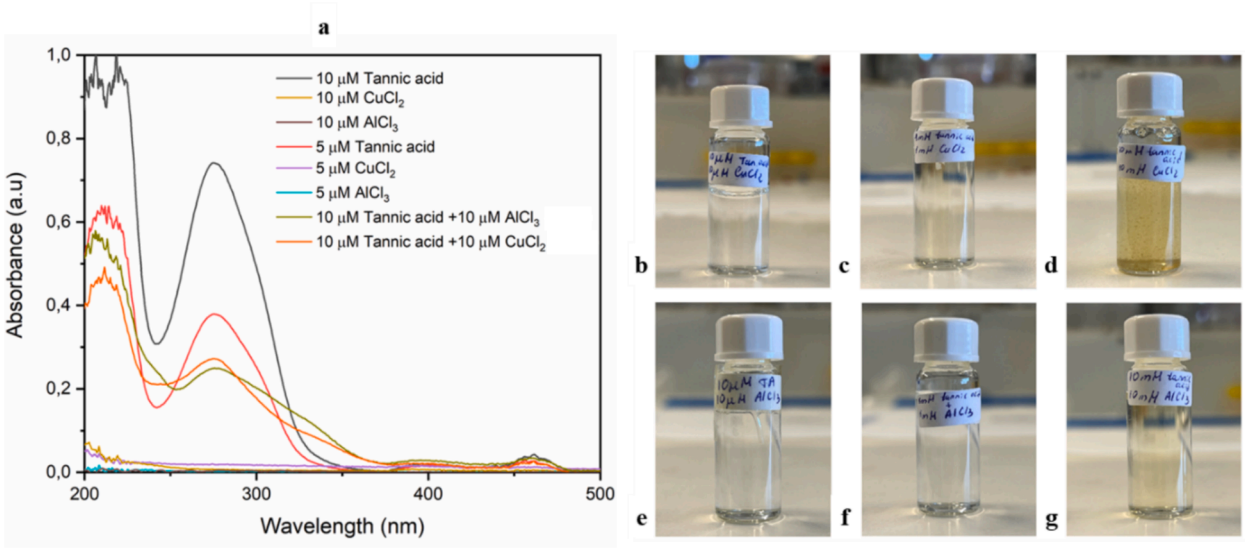

Fig. 4. (a) UV–Vis absorption spectra of Tannic acid, Cu, and Al chloride solutions and corresponding mixing solutions. Equimolar mixtures of tannic acid with $CuCl_2$ solution: (b) 10 μM, (c) 1 mM, and (d) 10 mM; and equimolar mixtures of tannic acid with $AlCl_3$ solutions: (e) 10 μM, (f) 1 mM, and (g) 10 mM.

and Cu cations. However, in the solutions (Fig. 4**b–g**), only the TA-$CuCl_2$ (10 mM) mixture revealed the formation of a precipitate, thereby indicating the formation of an insoluble Cu-tannate complex (Fig. 4**c**). At lower concentrations (1 mM and 1 μM), no visible precipitates were detected (Fig. 4**a,b**). By contrast, TA-$AlCl_3$ mixtures showed no visible precipitation at any concentration (Fig. 4**d–f**).

Therefore, although both Al and Cu ions interact among them by forming Al- [42] and Cu complexes [53], the observed black precipitates in Fig. 3 are related to the reaction between Cu^{2+} and tannate ions in the solution.

3.2. Long-term corrosion inhibition assessment of tannic acid on AA2024 alloy

3.2.1. Electrochemical impedance spectroscopy

Fig. 5 shows the Bode plots of the AA2024-T3 alloy following immersion in the study solutions for different immersion times (from 1 h to 7 days) (Nyquist plots of EIS spectra are depicted in **Figure S3**).

The electrochemical response in the Bode plot of the AA2024 alloy after 1 h of immersion in the blank solution (Fig. 5**a**) reveals two-time constants. The time constant at 10^2–10^0 Hz can correspond to the presence of the native oxide layer on the alloy surface, while the one at lower frequencies (10^{-1}-10^{-2} Hz) is related to the ongoing corrosion process. As the immersion time progresses, a continuous decrease in impedance magnitude values occurs (Fig. 1**a**), and displacement of time constants in the lowfrequency direction is observed (Fig. 1**a**). After 7 days of immersion, the two-time constants may be related to corrosion processes (intermediate frequency range) and mass-transport-related processes (low frequency range).

For the AA2024 alloy immersed in the TA solutions (1–7 days), two time constants were observed (Fig. 5**b–d**): (i) at intermediate frequencies (10^2-10^1) Hz, associated with the presence of the oxide protected with the tannate-rich film, and (ii) at low frequencies (10^0-10^{-2}) Hz, the electrochemical activity associated with corrosion processes.

For the AA2024 alloy immersed in the TA solutions (1–7 days), two time constants were observed (Fig. 5**b–d**): (i) at intermediate frequencies (10^2-10^1) Hz, associated with the presence of the oxide protected with the tannate-rich film, and (ii) at low frequencies (10^0-10^{-2}) Hz, the electrochemical activity associated with corrosion processes.

At low frequencies (10^0–10^{-2}) Hz, after 1 h of immersion (Fig. 5**a**), the impedance modulus at 10^{-2} Hz for the AA2024 alloy in the blank solution is almost two orders of magnitude lower (~10^4 Ω cm^2) than that observed in TA solutions (~$7{\cdot}10^5$ Ω cm^2) (Fig. 5**b–d**). However, after 1 day of immersion, the impedance modulus decreases for both the blank solution (~$3{\cdot}10^3$ Ω cm^2) and the TA solutions (~10^5 Ω cm^2).

Then, after 4 days of immersion, the impedance moduli in the TA-based solutions converged to similar values. From the fourth day of immersion onwards, a noticeable impedance decrease was observed in the 10 mM TA solution (Fig. 5**d**) compared to 0.1 and 1 mM TA solutions (Fig. 5**b, c**). It is worth mentioning that this decrease in the low frequency impedance for 10 mM TA when compared to 0.1 and 1 mM TA, is consistent with the results of PDP performed after 24 h of immersion: the protective layer formed in the substrate revealed to be the least protective among the three concentrations studied [10,17].

To further address the distinct impedance moduli observed with varying TA concentrations, equivalent circuits were used to fit the experimental data from the AA2024 alloy immersed in both the blank (Fig. 6**a**, Table 3) and TA-based solutions (Fig. 6**b**, Table 3).

In these circuits, Rsol represents the electrolyte resistance, and constant phase elements (CPE) were used instead of capacitances to accommodate the non-ideal characteristics of the system. In both equivalent circuits, R-ox is the oxide layer resistance, and CPE-ox and n_{ox} are the constant phase element (CPE) parameters used to describe the behavior of the outer oxide layer. R-ct is the charge transfer resistance, and CPE-dl and n-dl are the parameters for the double-layer capacitance. In the case of the blank solution fitting, a Warburg element (W) was included to account for ionic diffusion through the oxide layer on the alloy surface. The obtained fit parameters are presented in Table 3.

Fig. 7 represents the changes in the parameters of the outermost oxide layer (CPE-ox), charge transfer resistance (R-ct), and double-layer capacitance (CPE-dl) as a function of immersion time.

Overall, the properties of the oxide layer, including capacitance and resistance, are critical factors influenced by the passive film thickness, dielectric constant, and resistance to Cl^- ion penetration into the bare material [32,43]. As depicted in Fig. 7**a**, the similar oxide capacitances observed for the AA2024 alloy immersed in all TA solutions suggest the formation of a protective tannate-rich oxide layer on the AA2024 surface.

However, several differences were observed in the responses of charge transfer resistance (R_{ct}) and double-layer capacitance (CPE-dl) of the alloy exposed to the different TA solutions. Namely, the electrochemical response of the alloy immersed in 0.1 and 1 mM TA solutions led to a higher charge transfer resistance (Fig. 7**b**) and lower double-

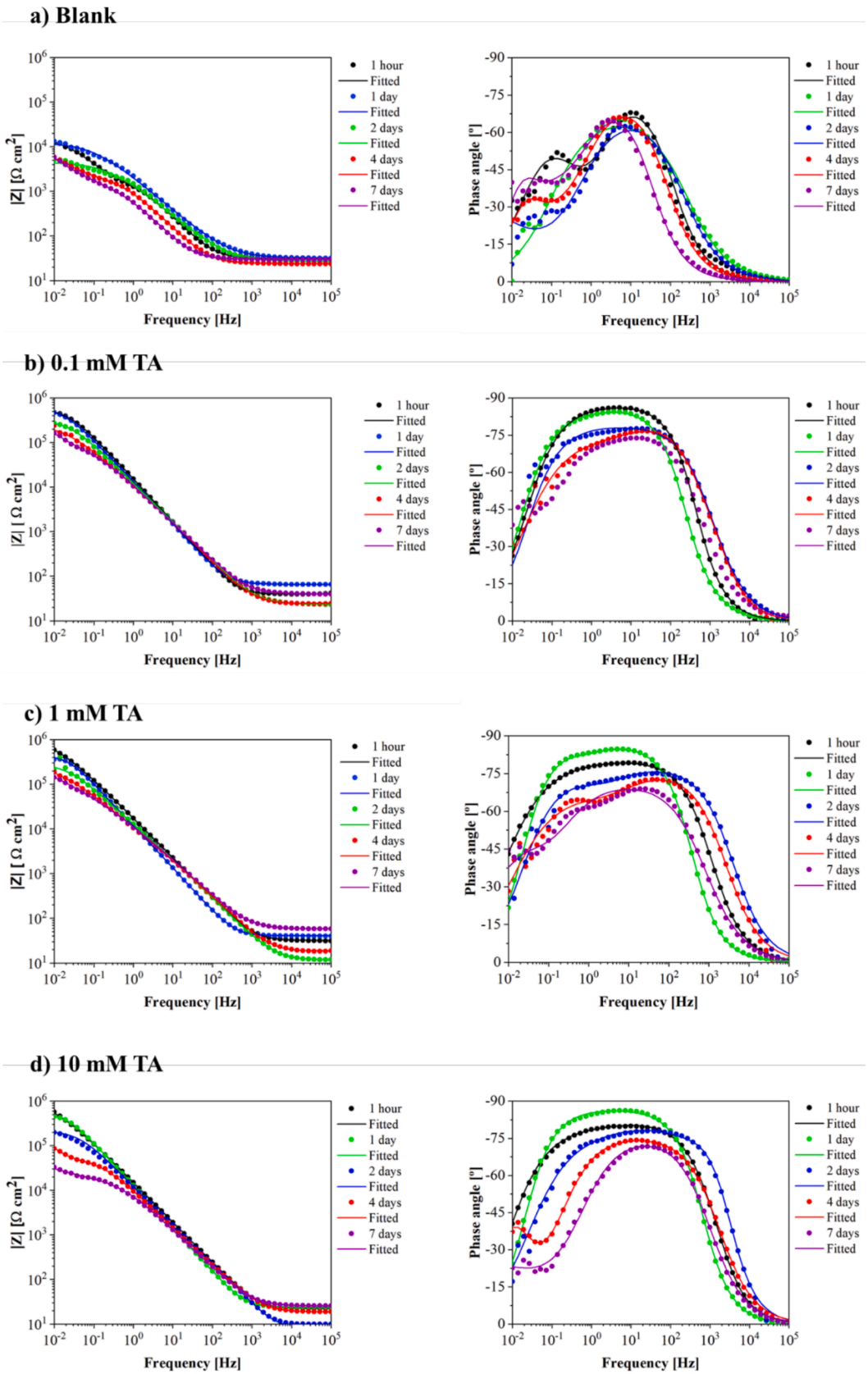

Fig. 5. Bode plots of AA2024 alloy after different immersion times in naturally aerated (a) 50 mM NaCl solutions with different TA concentrations: (b) 0.1 mM TA, (c) 1 mM TA, and (d) 10 mM TA.

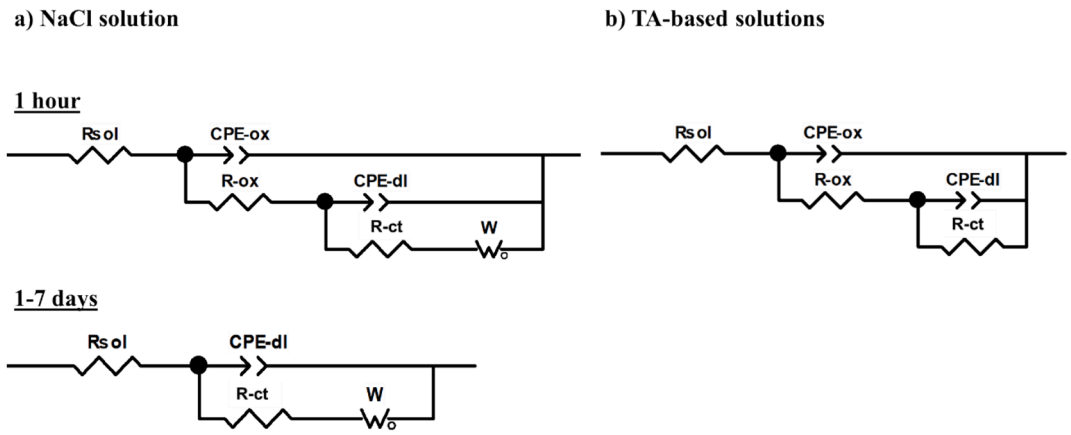

Fig. 6. Equivalent circuits to fit the experimental EIS data of the AA2024 in naturally aerated (a) 50 mM NaCl solution and (b) TA-containing solutions.

Table 3
Fitted electrical parameters of the AA2024 after the tested immersion times in naturally aerated 50 mM NaCl solutions with different TA concentrations.

Solution	Immersion time [days]	Rsol [Ω cm^2]	R-ox [KΩ cm^2]	CPE-ox [F s^{n-1} cm^{-2}]	nox	R-ct [KΩ cm^2]	CPE-dl [F s^{n-1} cm^{-2}]	ndl	W [mS $s^{1/2}$ cm^{-2}]
Blank	1 h	9.2	1.3	$2.0{\cdot}10^{-4}$	0.9	3.1	$1.1{\cdot}10^{-4}$	0.6	0.8
	1	31.9	–	–	–	11.9	$5.5{\cdot}10^{-4}$	0.7	5.4
	2	26.6	–	–	–	4.5	$5.3{\cdot}10^{-4}$	0.6	28.0
	4	23.9	–	–	–	1.7	$3.1{\cdot}10^{-3}$	0.9	1.0
	7	29.7	–	–	–	1.0	$2.1{\cdot}10^{-3}$	0.9	0.9
0.1 mM TA	1 h	7.7	138.8	$2.7{\cdot}10^{-5}$	0.9	428.0	$9.4{\cdot}10^{-6}$	0.9	–
	1	15.7	111.1	$3.5{\cdot}10^{-5}$	0.9	376.4	$2.1{\cdot}10^{-6}$	0.9	–
	2	24.2	57.3	$6.7{\cdot}10^{-5}$	0.9	252.7	$3.9{\cdot}10^{-6}$	0.9	–
	4	4.2	75.5	$7.2{\cdot}10^{-5}$	0.9	300.0	$1.6{\cdot}10^{-6}$	0.8	–
	7	39.7	96.2	$2.1{\cdot}10^{-4}$	0.8	210.3	$2.4{\cdot}10^{-5}$	0.9	–
1 mM TA	1 h	31.0	455.5	$6.0{\cdot}10^{-5}$	0.9	588.7	$6.2{\cdot}10^{-5}$	0.8	–
	1	9.3	40.9	$1.9{\cdot}10^{-5}$	0.9	415.1	$2.2{\cdot}10^{-5}$	0.9	–
	2	11.5	54.8	$1.0{\cdot}10^{-4}$	0.8	234.8	$9.1{\cdot}10^{-5}$	0.8	–
	4	16.5	88.5	$1.1{\cdot}10^{-4}$	0.8	260.3	$2.8{\cdot}10^{-5}$	0.7	–
	7	46.2	74.4	$2.4{\cdot}10^{-4}$	0.8	250.0	$4.7{\cdot}10^{-5}$	0.7	–
10 mM TA	1 h	22.55	37.9	$1.0{\cdot}10^{-5}$	0.9	919.4	$2.5{\cdot}10^{-5}$	0.7	–
	1	21.8	27.7	$2.6{\cdot}10^{-5}$	0.9	178.5	$9.2{\cdot}10^{-5}$	0.8	–
	2	8.3	26.5	$1.4{\cdot}10^{-5}$	0.9	215.0	$3.0{\cdot}10^{-4}$	0.8	–
	4	18.4	16.0	$2.1{\cdot}10^{-4}$	0.8	172.5	$8.4{\cdot}10^{-4}$	0.9	–
	7	25.0	8.1	$2.8{\cdot}10^{-4}$	0.8	18.3	$7.0{\cdot}10^{-4}$	0.9	–

layer capacitance (Fig. 7**c**) values compared to those formed in the 10 mM TA solution (Fig. 7**b,c**). In the 10 mM TA solution, a progressive decrease in the resistance was observed after the fourth day of immersion, reaching values similar to those observed in the blank solution (Fig. 7b). This trend suggests increased hydration, heterogeneities, and enhanced conductivity as the layer degrades, thus showing reduced passivation of the aluminium matrix in the 10 mM TA solution compared to 0.1 and 1 mM TA solutions. This could be linked to the formation of unstable passive layer modifications at the metal interface, diffusion-controlled processes and the adsorption of intermediate-charged species. As a result, an acceleration in the kinetics of the overall corrosion process in the presence of Cl^- ions is observed [22,40].

To correlate the findings of the EIS tests with the properties of the corrosion product layer, Fig. 8 shows the surface appearance after different immersion times. Notably, the AA2024 alloy exposed to the blank solution showed severe corrosion with extensive pitting after just 1 h of immersion (Fig. 8a). In contrast, samples immersed in TA-based solutions showed minimal corrosion damage after 1 day of immersion, indicative of the protective effect of chemisorbed tannate anions on the AA2024 alloy, regardless of the TA concentration (*Section 3.1*).

After 4 days of immersion, the formation of a brown-colored corrosion product layer was observed on the AA2024 alloy in all the studied solutions (Fig. 8**b**), consistent with the EIS results (Figs. 5, 6; Table 2) and the immersion test of pure Al in 1 Mm TA solution (**Figure S2**). The formation of this brown-colored layer is likely associated with the incorporation or interaction of the chemisorbed tannate anions on the forming aluminium hydroxide-rich corrosion product layer, predominantly bayerite (β-$Al(OH)_3$ [58]). Samples immersed in 10 and 1 mM TA solutions displayed a denser and more intensely colored corrosion product layer (Fig. 8**b**) compared to that in 0.1 mM TA solution. This difference may be attributed to a higher content of tannate species in the developing corrosion product layer (as discussed further in *Section 3.3*).

Besides, the noticeable pitting in the Cu-rich phases (both in terms of number and size) after immersion in the 10 mM TA solution (Fig. 8) confirms the limited stability of the product layer. This observation also correlates with the observed decrease in overall Rct and increase in CPE-dl from the fourth day of immersion (Figs. 6, 7).

While these findings help explain the different properties of the formed corrosion product layers in the studied TA solutions, the detailed morphological and compositional features of the AA2024 alloy after immersion in the tested solutions remain undisclosed. Hereto, the surface morphology of AA2024 immersed in TA solutions after long-term exposure times was carefully analyzed.

3.3. Characterization of AA2024 alloy after long-term immersion in the study solutions

To analyze the morphology and chemical composition of the

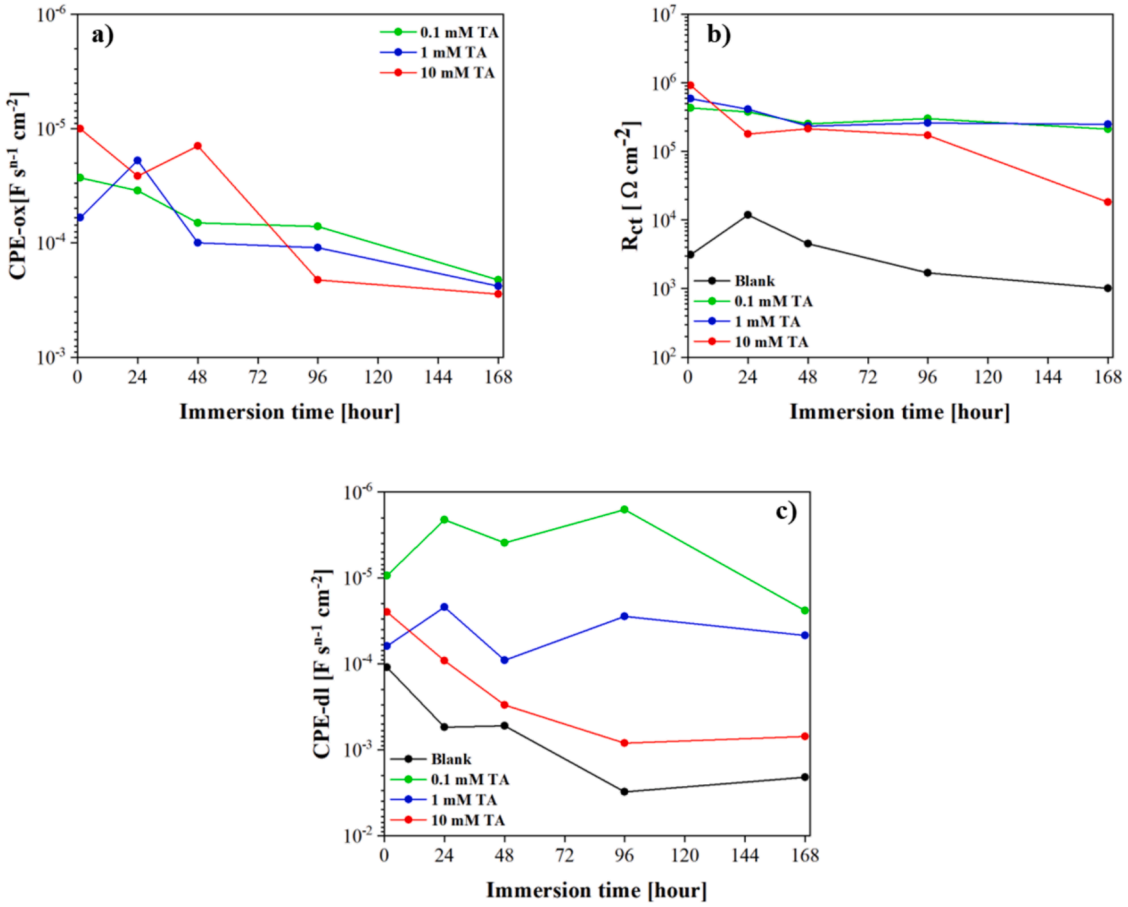

Fig. 7. Evolution of (a) oxide capacitance, (b) charge transfer resistance, and (c) double-layer capacitance of the AA2024 alloy during the studied immersion times in the study solutions.

corrosion product layers, SEM (Fig. 9) and EDS analysis (Table 4) were performed on the AA2024 alloy after 7 days of immersion in the study solutions.

As shown in Fig. 9**a–b**, the AA2024 sample exposed to the blank solution revealed a heterogeneous corrosion product layer with numerous bright deposits, presumably aluminum oxides/hydroxides, mostly bayerite (β-$Al(OH)_3$) (Table 4) [58].

In contrast, the AA2024 alloy exposed to the TA solutions revealed the formation of a cracked and heterogeneous corrosion product layer over the aluminum matrix (Fig. 9**c–k**). A common feature of these samples is the presence of several pits with higher Cu content in the center and its surroundings (represented by the green color in Fig. 9**d,g, j**). This is usually associated with the S-phase dealloying and Cu redeposition processes [16,43]. The sample exposed to the 0.1 mM TA solution (Fig. 9 **c-e**) displayed a more heterogeneous corrosion product layer compared to those formed in the 1–10 mM TA solutions. This may suggest that, although tannate anions interact with the Al matrix, their efficient incorporation onto the corrosion product layer may depend upon the TA/NaCl concentration ratio.

The EDS analysis of the Al matrix of the AA2024 after immersion in the study solutions (Table 4) reveals a comparable amount of Mg and Cu from the base material, regardless of the tested solution. However, different content of Al, C, and O were detected as a function of the TA concentration in the solutions.

For the AA2024 alloy immersed in the blank solution, the corrosion product layer is primarily composed of Al and O, indicating the formation of aluminum oxide/hydroxides. Conversely, the higher C content in the AA2024 samples immersed in TA-based solutions (Table 4) is likely due to the incorporation of tannates into the aluminum-(hydr)oxide corrosion product layer (represented by the blue color in Fig. 9**d,g,j**).

To ascertain the interaction of tannate anions with the corrosion product layer, Raman analysis was performed on AA2024 samples after 7 days of immersion in the blank and TA-based solutions (Fig. 10a). Note that the selected Raman region highlights the different signals as a function of the tested TA solution.

The AA2024 samples immersed in all the studied TA solutions showed the same signal in the (1600–1570) cm^{-1} range. This region is usually associated with aromatic ring vibrations, *i.e.*, in-plane bending/stretching of C–H and C-OH bonds of the benzene ring [41,59]. These bonds may result from the initial chemisorption of tannate anions on the Al surface and their further incorporation into the corrosion product layer as Al(hydr)oxides/tannates-rich precipitates, as stated in *Section 3.1-3.2*. This is in agreement with several studies in which it has been reported that the interaction between tannin-bound alumina [60] and tannic acid with different steels [28,41,61] results in a Raman signal broadening in this range.

This shared feature reveals that the corrosion products exhibit comparable chemical compositions. Notwithstanding, a proportional decrease in the Raman signal is observed at lower TA concentrations. This may be associated with a lower concentration of tannates in the corrosion product layer [41], as shown in the EDS analysis (Table 4).

For the AA2024 alloy exposed to the 10 mM TA solution, an additional signal at 1340 cm^{-1} corresponds to the C–H deformation in the aromatic ring plane [28,41,61]. The presence of this additional band may be associated with a higher content of tannates in the corrosion product layer [41,59].

Since the tannate content in the corrosion product layer can influence its morphology, composition, and corrosion resistance, it may also

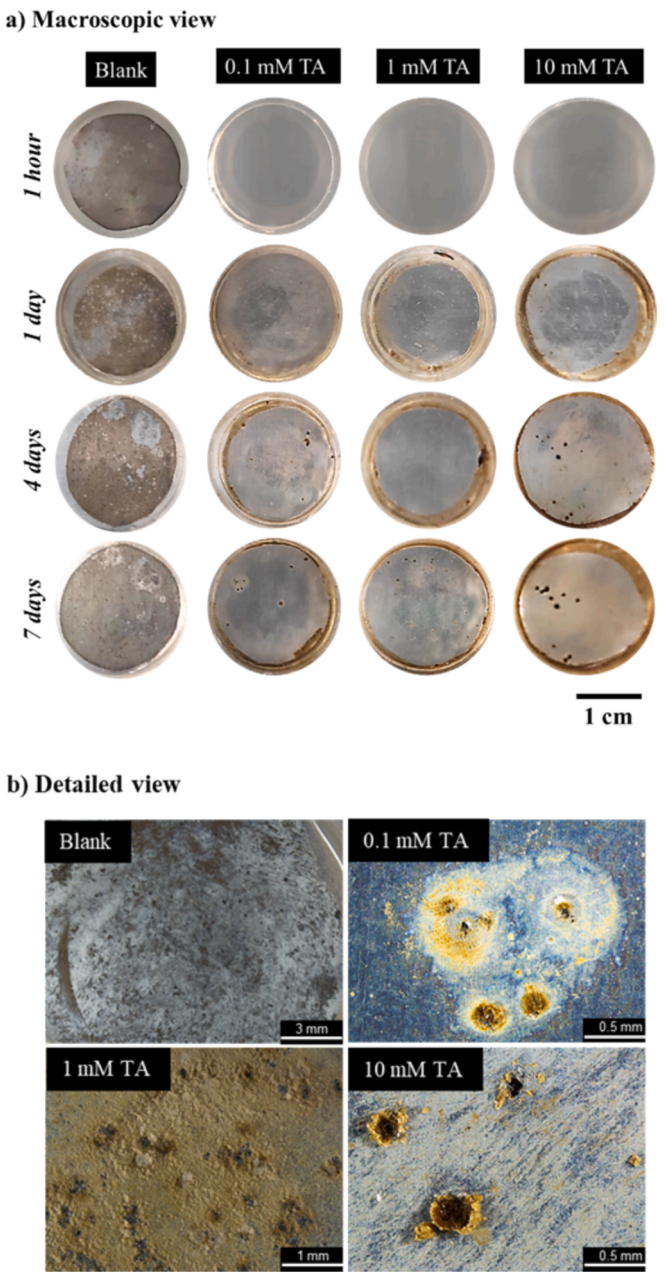

Fig. 8. (a) Macroscopic, and (b) detailed view of the AA2024 samples after 7 days of immersion in naturally aerated 50 mM NaCl solutions with different TA concentrations.

affect water uptake. To investigate this, the water contact angle (WCA) deviations of the AA2024 alloy immersed in the study solutions were evaluated as a function of immersion time (Fig. 10b).

Overall, the AA2024 alloy shows high hydrophilicity, with contact angle values below 90 degrees throughout the immersion period, regardless of the solution used. During the first 1 day of immersion, the AA2024 alloy exposed to the blank solution exhibited higher contact angle values (~40°) than those for TA-containing solutions (~20–30°). This suggests that the short-term interaction between tannate anions and the aluminum matrix and secondary phases leads to enhanced passivity rather than general hydrophobic protection. This interpretation of the passive behaviour aligns with the findings from SKPFM (Fig. 2) and SVET analysis on the Al matrix (Fig. 3).

Following the initial 1 day, the WCA values for the AA204 alloy exposed to the TA-based solutions showed a significant rise (~60–70°) compared to that of the blank solution (~20°). This trend prevailed throughout the studied immersion period, regardless of the TA concentration used. This phenomenon may indicate a short-term enhanced passivity by the tannate anions with the Al matrix (as discussed in *Section 3.2*), and their further incorporation into the forming corrosion product layer as the corrosion progresses, as shown in Raman analysis (Fig. 10**a**).

These differences in hydrophobicity and the heterogeneous morphology of the corrosion product layers raise the inquiry of a possible correlation between such variations and the surface roughness of the corrosion product layers. Since the susceptibility of AA2024-T3 to localized corrosion is usually linked to increased surface roughness [10], 3D topographical maps of the AA2024-T3 alloy after 7 days of immersion in the study solutions are shown in Fig. 11.

As depicted, the 3D topographical maps illustrate variations in surface height across the sample area. For AA2024 exposed to the blank solution (Fig. 11), corrosion products and dissolved areas were evident throughout the surface.

In contrast, the 3D maps of AA2024-T3 samples exposed in TA-based solutions show an almost intact aluminum surface after immersion, regardless of the TA concentration used (Fig. 11). Regarding surface roughness, Table 5 summarizes the quantitative roughness results (Ra, Sa) of AA2024 after immersion in the study solutions.

As expected, AA2024 immersed in TA-based solutions showed significantly lower roughness values compared to those from the blank solution. Notably, AA2024 immersed in diluted TA solutions exhibited roughness values comparable to the bare AA2024 alloy. However, in the case of the 10 mM TA solution, slightly higher roughness values may be attributed to the heterogeneous tannate-based corrosion product layer, as shown in OM analysis (Fig. 8).

Based on the present findings and the distinct corrosion resistance of the AA2024 alloy in TA-containing solutions, it is possible to further discuss the inhibition mechanism of tannic acid on the AA2024 alloy.

3.4. Corrosion mechanism of tannic acid for AA2024 alloy in saline medium

Fig. 12 illustrates the schematic representation of the proposed mechanism of tannic acid inhibition for the AA2024 alloy. This mechanism is underpinned by findings from this study and the already-known corrosion mechanism of AA2024 alloy in saline solutions at neutral pH [2,8,43,45]. It should be noted that, although the proposed mechanism is summarized in two stages for clarity, both processes occur simultaneously.

In Stage I (Fig. 12), initial contact of the AA2024 alloy with a tannic-free saline environment leads to the rupture of the passive film by chloride ions, especially in the Cu-rich secondary phases, where the oxide film is thinner and more brittle. Subsequent water uptake initiates a chemical reaction involving aluminum from the matrix (**1**) and magnesium from the secondary phases (**2**).

$$2Al(s) + 6H_2O(l) \rightarrow 2Al^{3+}(aq) + 6OH^-(aq) + 3H_2(g)\uparrow \quad (1)$$

$$Mg(s) + 2H_2O(l) \rightarrow Mg^{2+}(aq) + 2OH^-(aq) + H_2(g)\uparrow \quad (2)$$

Simultaneously, in the presence of oxygen and under neutral pH conditions, oxygen reduction occurs at the Cu-rich S-phase particles, inducing a localized pH increase in these areas (**3**). Simultaneously, dissolved oxygen also facilitates copper oxidation (**4**) and the surface enrichment of the S-phase with copper hydroxide (if Cu is electrically disconnected from the S-phase).

$$O_2(aq) + 2H_2O(l) + 4e^- \rightarrow 4OH^-(aq) \quad (3)$$

$$2Cu(s) + O_2(g) + 2H_2O(l) \rightarrow 2Cu(OH)_2(aq) \quad (4)$$

On this basis, the oxidation of the Cu-containing secondary phases leads

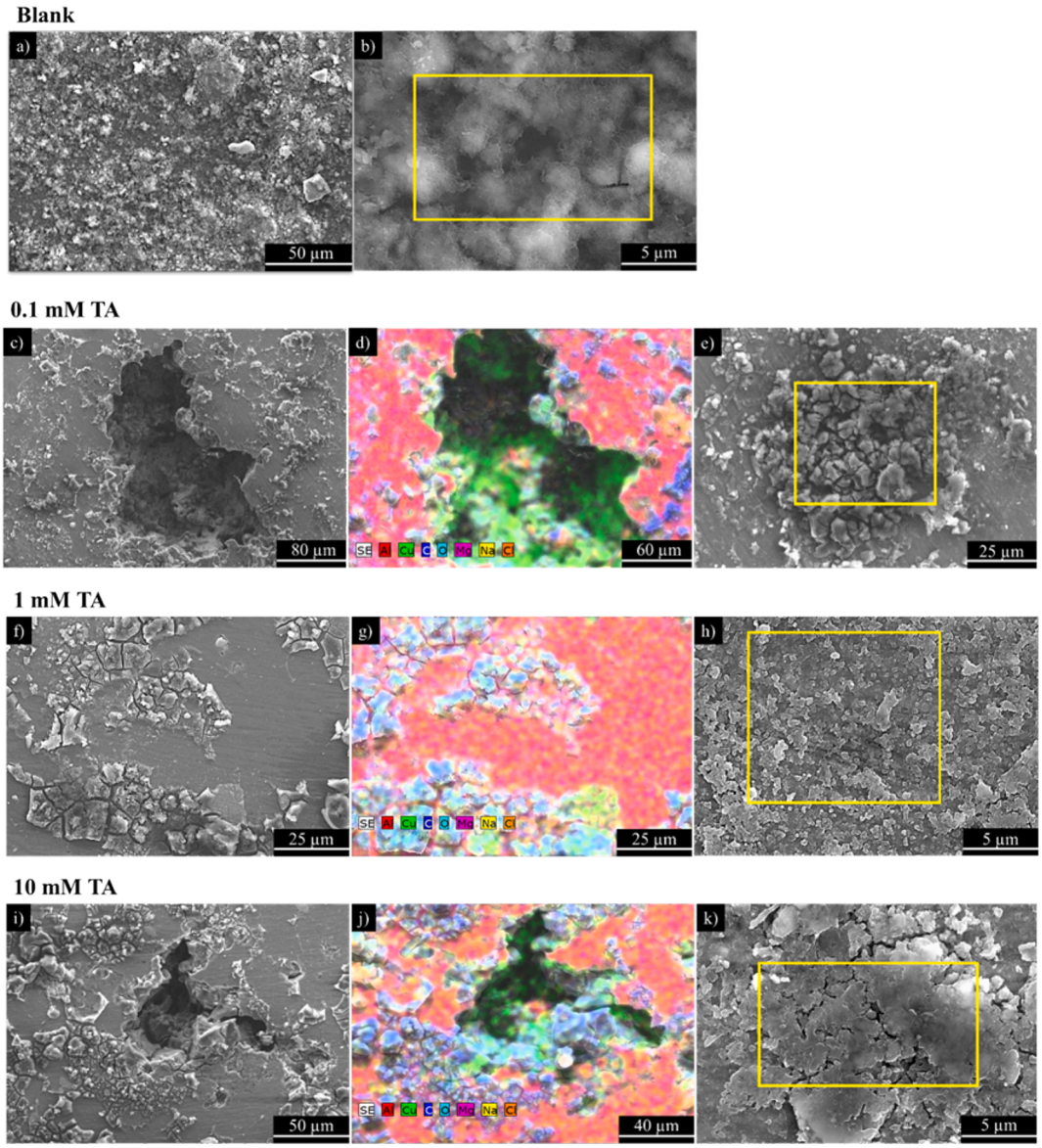

Fig. 9. Scanning electron micrographs of the AA2024 samples after 7 days of immersion in naturally aerated 50 mM NaCl solutions: (a,b) blank; (c-e) 0.1 mM; (f-h) 1 mM; and 10 mM (i-k) TA solutions.

Table 4
EDS analysis (at.%) of the AA2024 samples after 7 days of immersion in naturally aerated 50 mM NaCl (blank) and TA-based solutions. Matrix analysis have been performed at lower magnifications. Deposit locations are denoted on SEM images in Fig. 9.

Solution	Zone	C	O	Mg	Al	Cu
Blank	Matrix	17.2	49.4	0.4	32.3	0.7
	Deposit	18.3	50.1	0.4	30.6	0.6
0.1 mM	Matrix	32.6	2.4	1.1	62.9	0.9
	Deposit	49.8	6.9	0.8	41.9	0.7
1 mM	Matrix	49.4	4.9	0.8	44.4	0.6
	Deposit	45.7	20.9	0.7	32.6	0.1
10 mM	Matrix	47.4	9.9	0.8	41.3	0.6
	Deposit	46.7	21.9	0.6	30.4	0.4

to the formation of a gradient of OH^- ions between the secondary phase surface and the saline solution. Therefore, Al^{3+} cations formed from the oxidation of the matrix (**1**) are also likely to react with the OH^- ions (**5**), resulting in the formation of insoluble $Al(OH)_3$.

$$Al^{3+}(aq) + 3OH^-(aq) \rightarrow Al(OH)_3(s)\downarrow \quad (5)$$

In the case of AA2024 samples immersed in TA solutions, as discussed in *Section 3.1*, the initial passive response of the aluminum matrix and secondary phases observed in SVET and SKPFM analyses was attributed to the chemisorption of tannate anions (O-R groups) on both the Al matrix (**6**) [42] and Cu-rich secondary phases (**7**) [54,55] (depicted in Stage I; Fig. 12).

It should be noted that while tannate chemisorption occurs predominantly in the early stages of immersion, the corrosion process involving oxidation of both the Al matrix and the secondary phases proceeds simultaneously (Stage II; Fig. 12), as demonstrated in the SVET analysis (Fig. 3; *Section 3.1*). This results in the formation of a brown-colored oxide layer on the Al matrix. Namely, the resultant oxide layer can be described as a mixture of tannate and aluminum hydroxide as corrosion progresses (marked in Stage II; Fig. 12), as indicated by Raman analysis (Fig. 10**a**).

However, although this mechanism is applicable across all studied TA solutions on the AA2024 alloy, the presence of pitting (Stage II; Fig. 12) and their different corrosion performance (*Section 3.2*) denotes

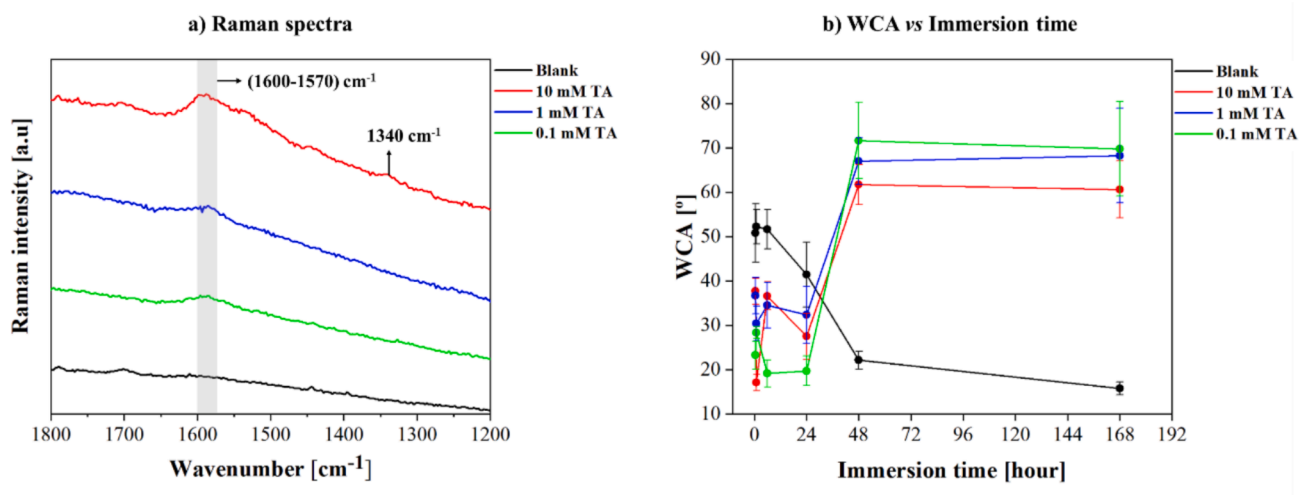

Fig. 10. (a) Raman analysis and (b) water contact angle of the AA2024 samples after 7 days of immersion in naturally aerated 50 mM NaCl (blank) and TA-based solutions.

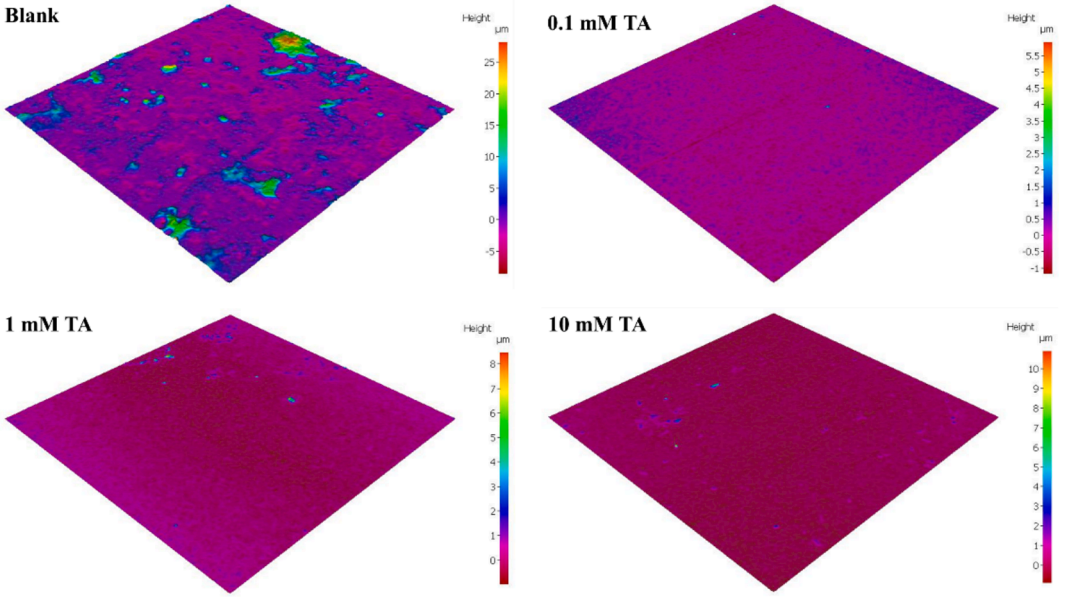

Fig. 11. 3D topographical maps of AA2024 surface after 7 days of immersion in naturally aerated 50 mM NaCl (blank) and TA-based solutions.

Table 5
Roughness values of AA2024 surface before and after 7 days of immersion in naturally aerated 50 mM NaCl (blank) and TA-based solutions.

	Ra (µm)	Sa (µm)
Bare AA2024 alloy	0.06 ± 0.01	0.10 ± 0.01
Solution		
Blank	0.80 ± 0.01	2.80 ± 0.70
10 mM TA	0.12 ± 0.01	0.10 ± 0.02
1 mM TA	0.05 ± 0.01	0.12 ± 0.02
0.1 mM TA	0.05 ± 0.01	0.10 ± 0.02

that the interaction of tannate anions with the Al matrix and the secondary phases is different according to the tested TA solutions. It is well-known that pitting in 2024 alloy is linked to Al dissolution around Cu-containing secondary phases, which typically occurs under low pH conditions due to the hydrolysis of Al^{3+} (**5**) [2]. Therefore, at low pH values, the OH groups of tannate anions in the surroundings of the secondary phases may not be fully dissociated, affecting their adsorption ability [22,53].

By comparison, while the 10 mM TA solution exhibited the best cathodic inhibition performance during the first 1 day of immersion (*Section 3.1*), the long-term EIS results for the 0.1 and 1 mM TA solutions demonstrated better passivation of the Al matrix. This suggests that the higher concentration of tannate anions in the 10 mM TA solution may lead to a lesser increase in pH around the Cu-rich secondary phases compared to pure NaCl solutions after the first 1 day of immersion, thus inhibiting pit formation.

However, over time, the ability to passivate the Al matrix is the lowest at 10 mM TA. Namely, the formation of insoluble Cu-tannate precipitates at a concentration of 10 mM (Fig. 4) may confirm that tannate anions may not effectively inhibit pitting near the Cu-rich secondary phases at 10 mM TA, *i.e.*, the Cu dissolution, and re-deposition in the formed pits is favored. This could explain the lower corrosion resistance for 10 mM TA after the long-term EIS test.

Besides, since the only difference between the passive layers formed in TA solutions lies in the higher tannate anion content in the corrosion product layer of the 10 mM TA solution (Fig. 10; Section 3.3), the

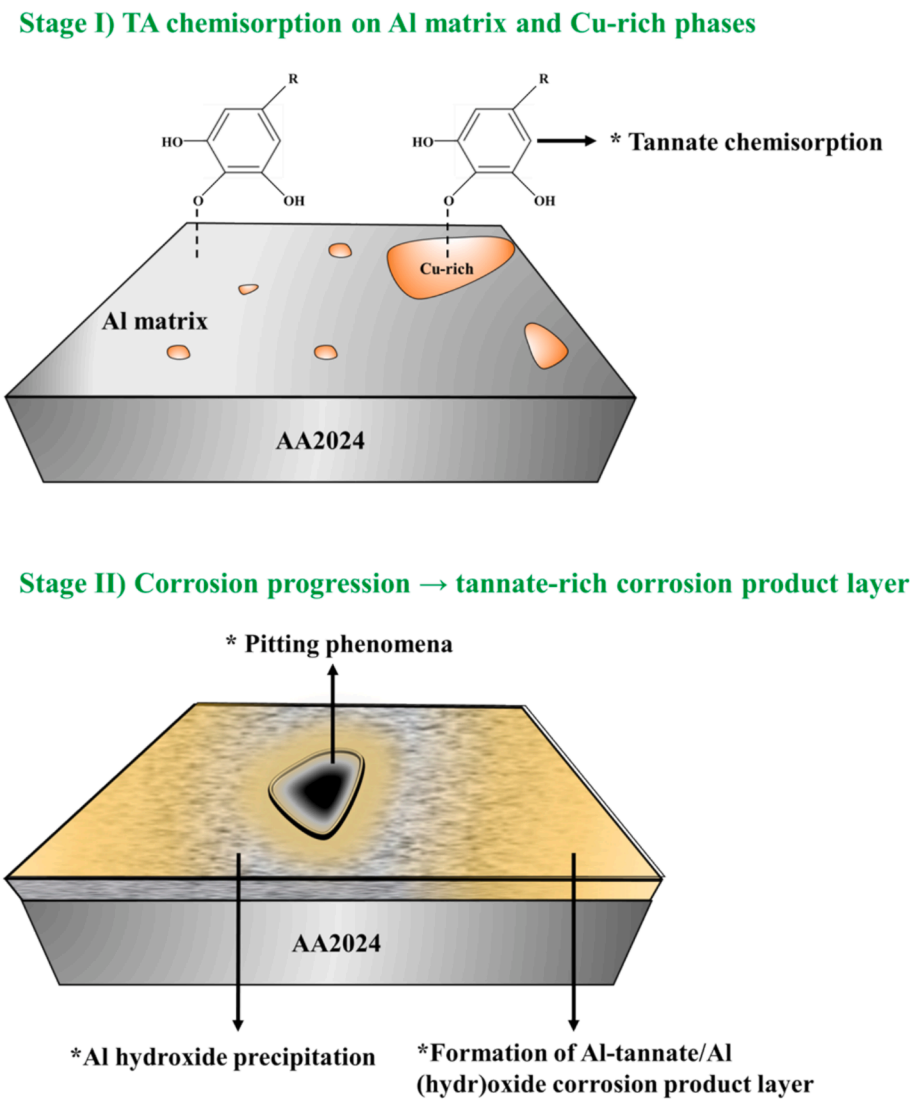

Fig. 12. Schematic illustration for inhibition mechanism of tannic acid for the AA2024 alloy.

reduced corrosion resistance of the AA2024 sample may also be attributed to the instability of the formed corrosion layer.

These factors may account for the lower corrosion resistance in long-term EIS tests. Therefore, for the sake of comparison, although the proposed protection mechanism (Fig. 12) is common for all the tested solutions, the 1 mM TA solution provided a superior short- and long-term corrosion performance, thus being the most balanced choice for corrosion inhibition.

4. Conclusions and future perspectives

The main conclusions regarding the fundamentals of tannic acid and its corrosion-inhibiting performance on AA2024 alloy can be summarized as follows:

- Short-term corrosion (PDP) results reveal that 10 and 1 mM of TA is the optimal concentration range needed to achieve a notable inhibition on the AA2024 alloy.
- Short-term SKPFM analyses suggest the chemisorption of tannates on both the Al matrix and S-phase, thereby hampering the dissolution of both phases in a neutral saline medium.
- Short-term SVET analyses reveal that the anodic currents are considerably lower than those detected in the blank solution, thus indicating efficient tannate inhibition on the Cu-rich secondary phases in a neutral saline medium.
- The long-term exposure of AA2024 alloy in TA solutions results in the formation of a tannate-rich corrosion product layer with a higher water contact angle and lower roughness than the sample immersed in the blank solution.
- Long-term corrosion tests of AA2024 alloy in diluted (0.1 and 1 mM) TA solutions result in a corrosion-protective and stable Al-tannate-rich oxide layer. By contrast, in concentrated TA solutions (10 mM), the resultant corrosion product layer shows a higher tannate content, lower stability, and, as a consequence, low corrosion resistance.

The present findings reveal that tannic acid is an efficient corrosion inhibitor when it is present at low concentrations (0.1 and 1 mM) in saline medium. Therefore, tannic acid can be considered a highly available, eco-friendly, and cost-effective Cr-free inhibitor for AA2024 alloy. Nevertheless, further studies should address the incorporation of tannic acid or tannins in the most commonly used surface treatments in the aerospace industry (pre-treatments, primers, and paints) to match the stringent requirements of the aerospace industry.

CRediT authorship contribution statement

Rubén del Olmo: Writing – review & editing, Writing – original draft, Visualization, Validation, Software, Project administration, Methodology, Investigation, Funding acquisition, Formal analysis, Data curation, Conceptualization. **Alexandre Bastos:** Writing – review & editing, Visualization, Validation, Software, Methodology, Investigation, Formal analysis, Data curation, Conceptualization. **Kiryl Yasakau:** Writing – review & editing, Visualization, Validation, Software, Methodology, Investigation, Formal analysis, Data curation, Conceptualization. **Alesia Sushkova:** Writing – review & editing, Visualization, Validation, Methodology, Investigation, Formal analysis, Data curation. **Raúl Arrabal:** Writing – review & editing, Visualization, Validation, Supervision, Resources, Project administration, Investigation, Funding acquisition, Formal analysis, Conceptualization. **João Tedim:** Writing – review & editing, Visualization, Validation, Supervision, Resources, Project administration, Methodology, Investigation, Funding acquisition, Formal analysis, Conceptualization.

Declaration of competing interest

The authors declare that they have no known competing financial interests or personal relationships that could have appeared to influence the work reported in this paper.

Data availability

Data will be made available on request.

Acknowledgements/Funding

This work was developed within the scope of Project CICECO-Aveiro Institute of Materials, UIDB/50011/2020 (DOI 10.54499/UIDB/50011/2020), UIDP/50011/2020 (DOI 10.54499/UIDP/50011/2020), and LA/P/0006/2020 (DOI 10.54499/LA/P/0006/2020), financed by national funds through the FCT/MEC (PIDDAC). R. del Olmo acknowledges the financial support from the Margarita Salas CT18/22 post-doctoral grant. A. Bastos is funded by national funds (OE), through FCT - Fundação para a Ciência e a Tecnologia, I.P., in the scope of the framework contract foreseen in the numbers 4, 5, and 6 of article 23, of the Decree-Law 57/2016, of August 29, changed by Law 57/2017, of July 19. K. Yasakau acknowledges the FCT for the researcher grant (2021.00842.CEECIND). PhD grant of Alesia Sushkova is funded by the FCT and FSE- Fundo Social Europeu (2021.07744.BD). R. Arrabal acknowledges the support by PID2021-124341OB-C22 (MICINN/AEI/FEDER, UE).

Appendix A. Supplementary material

Supplementary data to this article can be found online at https://doi.org/10.1016/j.apsusc.2024.161434.

References

[1] C. Vargel, Chapter F.1 - Protection of aluminium, in: C. Vargel (Ed.), Corrosion of Aluminium, 2nd Edition, Elsevier, Amsterdam, 2020, pp. 383–443.
[2] K.A. Yasakau, M.L. Zheludkevich, M.G.S. Ferreira, 15 - Role of intermetallics in corrosion of aluminum alloys. Smart corrosion protection, in: R. Mitra (Ed.), Intermetallic Matrix Composites, Woodhead Publishing, 2018, pp. 425–462.
[3] K.K. Sankaran, R.S. Mishra, Chapter 4 - Aluminum Alloys, in: K.K. Sankaran, R. S. Mishra (Eds.), Metallurgy and Design of Alloys with Hierarchical Microstructures, Elsevier, 2017, pp. 57–176.
[4] P. Visser, H. Terryn, J.M.C. Mol, Aerospace coatings, in: Springer Series in Materials Science, 2016, pp. 315-372.
[5] D.B. Mitton, A. Carangelo, A. Acquesta, T. Monetta, M. Curioni, F. Bellucci, Selected Cr(VI) replacement options for aluminum alloys: a literature survey, 35 (2017) 365-381.
[6] K.D. Ralston, S. Chrisanti, T.L. Young, R.G. Buchheit, Corrosion inhibition of aluminum alloy 2024–T3 by aqueous vanadium species, J. Electrochem. Soc. 155 (2008) C350.
[7] L.D.G. Ltd., Surface treatment for applications in the aeronautics and aerospace industries, unrelated to Functional chrome plating or Functional chrome plating with decorative character, in: n.-c.r. ANALYSIS OF ALTERNATIVES (Ed.).
[8] S.V. Lamaka, M.L. Zheludkevich, K.A. Yasakau, M.F. Montemor, M.G.S. Ferreira, High effective organic corrosion inhibitors for aluminium alloy, Electrochim. Acta 52 (2007) (2024) 7231–7247.
[9] S. Marcelin, N. Pébère, Synergistic effect between 8-hydroxyquinoline and benzotriazole for the corrosion protection of aluminium alloy: A local electrochemical impedance approach, Corros. Sci. 101 (2015) (2024) 66–74.
[10] P. Visser, H. Terryn, J.M.C. Mol, On the importance of irreversibility of corrosion inhibitors for active coating protection of AA2024-T3, Corros. Sci. 140 (2018) 272–285.
[11] M. Machkova, E.A. Matter, S. Kozhukharov, V. Kozhukharov, Effect of the anionic part of various Ce(III) salts on the corrosion inhibition efficiency of AA2024 aluminium alloy, Corros. Sci. 69 (2013) 396–405.
[12] O. Sanni, C.A. Loto, A.P.I. Popoola, Inhibitive behaviour of zinc gluconate on aluminium alloy in 3.5 % Nacl Solution, Silicon 8 (2016) 195–200.
[13] Z. Li, P. Visser, A.E. Hughes, A. Homborg, Y. Gonzalez-Garcia, A. Mol, Review of the state of art of Li-based inhibitors and coating technology for the corrosion protection of aluminium alloys, Surf. Coat. Technol. 478 (2024).
[14] D.S. Chauhan, A.A. Sorour, V.S. Saji, M.A. Quraishi, Green corrosion inhibitors based on biomacromolecules and macrocycles: A review, Sustain. Chem. Pharm. 36 (2023) 101295.
[15] N. Chaubey, A. Savita, D.S. Qurashi, M.A.Q. Chauhan, Frontiers and advances in green and sustainable inhibitors for corrosion applications: A critical review, J. Mol. Liq. 321 (2021) 114385.
[16] T.G. Harvey, S.G. Hardin, A.E. Hughes, T.H. Muster, P.A. White, T.A. Markley, P. A. Corrigan, J. Mardel, S.J. Garcia, J.M.C. Mol, A.M. Glenn, The effect of inhibitor structure on the corrosion of AA2024 and AA7075, Corros. Sci. 53 (2011) 2184–2190.
[17] H. Gerengi, M. Solomon, M. Kurtay, G. Bereket, K. Gökşen, M. Yildiz, E. Kaya, Electrochemical and morphological assessments of inhibition level of 8-hydroxyl-quinoline for AA2024-T4 alloy in 3.5% NaCl solution, J. Adhes. Sci. Technol. 32 (2017) 1–17.
[18] P.A.I. Popoola, S. Omotayo, C.A. Loto, O.M. Popoola, Inhibitive action of ferrous gluconate on aluminum alloy in saline environment, Adv. Mater. Sci. Eng. 2013 (2013) 639071.
[19] B.L. Hurley, S. Qiu, R.G. Buchheit, Raman spectroscopy characterization of aqueous vanadate species interaction with aluminum alloy 2024–T3 surfaces, J. Electrochem. Soc. 158 (2011) C125.
[20] J. Li, B. Hurley, R. Buchheit, Inhibition Performance Study of Vanadate on AA2024-T3 at High Temperature by SEM FIB, Raman and XPS, J. Electrochem. Soc. 162 (2015) C219.
[21] S.V. Lamaka, B. Vaghefinazari, D. Mei, R.P. Petrauskas, D. Höche, M. L. Zheludkevich, Comprehensive screening of Mg corrosion inhibitors, Corros. Sci. 128 (2017) 224–240.
[22] C.S. Proença, B. Serrano, J. Correia, M.E. Araújo, Evaluation of tannins as potential green corrosion inhibitors of aluminium alloy used in aeronautical industry, Metals (2022).
[23] R. Sesia, S. Spriano, M. Sangermano, S. Ferraris, Natural polyphenols and the corrosion protection of steel: recent advances and future perspectives for green and promising strategies, Metals (2023).
[24] M. Faustin, A. Maciuk, P. Salvin, C. Roos, M. Lebrini, Corrosion inhibition of C38 steel by alkaloids extract of Geissospermum laeve in 1M hydrochloric acid: Electrochemical and phytochemical studies, Corros. Sci. 92 (2015) 287–300.
[25] S.A. Umoren, U.M. Eduok, Application of carbohydrate polymers as corrosion inhibitors for metal substrates in different media: A review, Carbohydr. Polym. 140 (2016) 314–341.
[26] P.B. Raja, M.G. Sethuraman, Natural products as corrosion inhibitor for metals in corrosive media — A review, Mater. Lett. 62 (2008) 113–116.
[27] J. Cho, S. Roy, A. Sathyapalan, M. Free, Z. Fang, Tannic acid selectively extracting titanium from ilmenite: experimental and theoretical investigation, J. Powder Metall. Mining 06 (2017).
[28] A. Espina, M.V. Cañamares, Z. Jurašeková, S. Sanchez-Cortes, Analysis of iron complexes of tannic acid and other related polyphenols as revealed by spectroscopic techniques: implications in the identification and characterization of iron gall inks in historical manuscripts, ACS Omega 7 (2022) 27937–27949.
[29] A.E. Fazary, M. Taha, Y.-H. Ju, Iron complexation studies of gallic acid, J. Chem. Eng. Data 54 (2009) 35–42.
[30] A.A. Rahim, E. Rocca, J. Steinmetz, M.J. Kassim, R. Adnan, M. Sani Ibrahim, Mangrove tannins and their flavanoid monomers as alternative steel corrosion inhibitors in acidic medium, Corros. Sci. 49 (2007) 402–417.
[31] G. Matamala, W. Smeltzer, G. Droguett, Comparison of steel anticorrosive protection formulated with natural tannins extracted from acacia and from pine bark, Corros. Sci. 42 (2000) 1351–1362.
[32] B. Qian, B. Hou, M. Zheng, The inhibition effect of tannic acid on mild steel corrosion in seawater wet/dry cyclic conditions, Corros. Sci. 72 (2013) 1–9.
[33] X. Zuo, W. Li, S. Mu, J. Du, Y. Yang, P. Tang, Investigation of composition and structure for a novel Ti–Zr chemical conversion coating on 6063 aluminum alloy, Prog. Org. Coat. 87 (2015) 61–68.
[34] J.V. Nardeli, C.S. Fugivara, M. Taryba, M.F. Montemor, S.J.L. Ribeiro, A. V. Benedetti, Novel healing coatings based on natural-derived polyurethane

modified with tannins for corrosion protection of AA2024-T3, Corros. Sci. 162 (2020) 108213.
[35] E. McCafferty, Validation of corrosion rates measured by the Tafel extrapolation method, Corros. Sci. 47 (2005) 3202–3215.
[36] C. Scheffey, Two approaches to construction of vibrating probes for electrical current measurement in solution, Rev. Sci. Instrum. 59 (1988) 787–792.
[37] A.C. Bastos, M.C. Quevedo, O.V. Karavai, M.G.S. Ferreira, Review—on the application of the scanning vibrating electrode technique (SVET) to corrosion research, J. Electrochem. Soc. 164 (2017) C973.
[38] W. Melitz, J. Shen, A.C. Kummel, S. Lee, Kelvin probe force microscopy and its application, Surf. Sci. Rep. 66 (2011) 1–27.
[39] M. Rohwerder, F. Turcu, High-resolution Kelvin probe microscopy in corrosion science: Scanning Kelvin probe force microscopy SKPFM versus classical scanning Kelvin probe SKP, Electrochim. Acta 53 (2007) 290–299.
[40] E. Kusmierek, E. Chrzescijanska, Tannic acid as corrosion inhibitor for metals and alloys, Mater. Corros. 66 (2015) 169–174.
[41] W. Xu, E.-H. Han, Z. Wang, Effect of tannic acid on corrosion behavior of carbon steel in NaCl solution, J. Mater. Sci. Technol. 35 (2019) 64–75.
[42] T. Kolusheva, M. Hristova, L. Costadinnova, Study of the complex formation reaction between Al(III) and tannic acid, J. Uni. Chem. Technol. Metall. 47 (2012) 570–573.
[43] K.A. Yasakau, M.L. Zheludkevich, S.V. Lamaka, M.G.S. Ferreira, Mechanism of corrosion inhibition of AA2024 by rare-earth compounds, J. Phys. Chem. B 110 (2006) 5515–5528.
[44] A. Kreta, M. Gaberšček, I. Muševič, Time-resolved in situ electrochemical atomic force microscopy imaging of the corrosion dynamics of AA2024-T3 using a new design of cell, J. Mater. Res. 36 (2021) 79–93.
[45] K. Yasakau, Application of AFM-based techniques in studies of corrosion and corrosion inhibition of metallic alloys, Corros. Mater. Degrad. (2020) 345–372.
[46] P. Schmutz, G.S. Frankel, Corrosion study of AA2024-T3 by scanning kelvin probe force microscopy and in situ atomic force microscopy scratching, J. Electrochem. Soc. 145 (1998) 2295.
[47] M. Pérez, M. García, G. Blustein, M. Stupak, Tannin and tannate from the quebracho tree: an eco-friendly alternative for controlling marine biofouling, Biofouling 23 (2007) 151–159.
[48] R. Hausbrand, M. Stratmann, M. Rohwerder, The physical meaning of electrode potentials at metal surfaces and polymer/metal interfaces: consequences for delamination, J. Electrochem. Soc. 155 (2008) C369.
[49] K.A. Yasakau, A.N. Salak, M.L. Zheludkevich, M.G.S. Ferreira, Volta potential of oxidized aluminum studied by scanning kelvin probe force microscopy, J. Phys. Chem. C 114 (2010) 8474–8484.
[50] Ö. Özkanat, B. Salgin, M. Rohwerder, J.M.C. Mol, J.H.W. de Wit, H. Terryn, Scanning kelvin probe study of (oxyhydr)oxide surface of aluminum alloy, J. Phys. Chem. C 116 (2012) 1805–1811.
[51] A. Henning, G. Günzburger, R. Jöhr, Y. Rosenwaks, B. Bozic-Weber, C. E. Housecroft, E.C. Constable, E. Meyer, T. Glatzel, Kelvin probe force microscopy of nanocrystalline TiO_2 photoelectrodes, Beilstein, J. Nanotechnol. 4 (2013) 418–428.
[52] K.A. Yasakau, A. Maltseva, S.V. Lamaka, D. Mei, H. Orvi, P. Volovitch, M.G. S. Ferreira, M.L. Zheludkevich, The effect of carboxylate compounds on Volta potential and corrosion inhibition of Mg containing different levels of iron, Corros. Sci. 194 (2022) 109937.
[53] P. Kraal, B. Jansen, K.G.J. Nierop, J.M. Verstraten, Copper complexation by tannic acid in aqueous solution, Chemosphere 65 (2006) 2193–2198.
[54] A.M. Beccaria, E.D. Mor, Inhibitive effect of tannic acid on the corrosion of copper in acid solutions, Br. Corros. J. 11 (1976) 156–160.
[55] M. Pérez, G. Blustein, M. García, B. del Amo, M. Stupak, Cupric tannate: A low copper content antifouling pigment, Prog. Org. Coat. 55 (2006) 311–315.
[56] N.A. Che Lah, P. Murthy, M.N. Mohd Zubir, The physical and optical investigations of the tannic acid functionalised Cu-based oxide nanostructures, Sci. Rep. 12 (2022) 9909.
[57] M.G. Albu, M.V. Ghica, M. Giurginca, V. Trandafir, L. Popa, C.M. Cotruț, C. Davila, Spectral characteristics and antioxidant properties of tannic acid immobilized on collagen drug-delivery systems, Chimie (2009).
[58] G. Lefèvre, M. Duc, P. Lepeut, R. Caplain, M. Fédoroff, Hydration of γ-alumina in water and its effects on surface reactivity, Langmuir 18 (2002) 7530–7537.
[59] A.S. Lee, P.J. Mahon, D.C. Creagh, Raman analysis of iron gall inks on parchment, Vib. Spectrosc 41 (2006) 170–175.
[60] S. Brehm, C. Himcinschi, J. Kraus, B. Bock-Seefeld, C. Aneziris, J. Kortus, Raman spectroscopic characterization of environmentally friendly binder systems for carbon-bonded filters, Adv. Eng. Mater. 24 (2021) 2100544.
[61] Å. Henrik-Klemens, F. Bengtsson, C.G. Björdal, Raman spectroscopic investigation of iron-tannin precipitates in waterlogged archaeological oak, Stud. Conserv. 67 (2022) 237–247.